

Spectrochimica Acta Part B: Atomic Spectroscopy

An advanced analytical assessment of rare earth element concentration, distribution, speciation, crystallography and solid-state chemistry in fly ash

--Manuscript Draft--

Manuscript Number:	SAB_2020_128R3
Article Type:	Research Paper
Keywords:	Fly ash; Nigeria; monazite; synchrotron radiation.; Rare Earth Elements
Corresponding Author:	Ilemona Okeme University of Bristol Bristol, United Kingdom
First Author:	Ilemona Cornelius Okeme
Order of Authors:	Ilemona Cornelius Okeme Peter George Martin Christopher Jones Rich Crane Theophilus Ile Ojonimi Konstantin Ignatyev Thomas Bligh Scott
Abstract:	<p>Fly ash represents a promising alternative source of rare earth elements (REE). However, information on REE containing mineral phases and their association with other fly ash components, vital for REE recovery from fly ash, is currently lacking. Herein, the mass fraction, distribution, crystallography and solid-state chemistry of REE, U and Th in Nigerian simulated fly ash samples were characterised using a range of laboratory and synchrotron x-ray based analytical techniques to underpin future extraction methodologies. Inductively coupled plasma mass spectrometry following full-acid digest of forty-five samples revealed recoverable average total REE content which ranged between 442 mgkg⁻¹ and 625 mgkg⁻¹, comprising over 30wt% of the critical REE Nd, Eu, Tb, Dy, Y and Er. These REE within the fly ash samples were found to be most frequently associated with discrete monazite, xenotime and Y-bearing zircon mineral particles, with the former the most detected, which could be beneficiated through gravity separation. Analysis of monazite particles isolated from the composite samples through a complimentary suite of analytical synchrotron radiation techniques revealed a core-shell pattern, with the shell rich in colocalised Ce, Nd and La, and the core enrich in both U and Th. Ce in monazite was found to exist in a mixed trivalent and tetravalent oxidation state, with the monazite structure amorphized due to the high temperature combustion process. Such results demonstrate the strong co-association and physical distribution of REE, U and Th within monazite in fly ash; knowledge of which can subsequently be used to optimise or develop a more selective, cost-effective and environmentally friendly solvent extraction methodology, by targeting the strongly colocalised and surface bound REE in fly ash monazite particles.</p>
Suggested Reviewers:	Ian Graham i.graham@unsw.edu.au He has authored a good number of papers on coal geology and rare earths in top journals. Zhenxuan Wang zhenxuan.wang@duke.edu He has authored papers on rare earths in coal and coal ash materials. Avner Vengosh vengosh@duke.edu He has published papers on coal and fly ash in top journals
Opposed Reviewers:	

Response to Reviewers:	
-------------------------------	--



Mr. Ilemona C. Okeme
Interface Analysis Centre
HH Wills Physics Laboratory
University of Bristol
Tyndall Avenue
Bristol
BS8 1TL
Email: io17820@bristol.ac.uk
Tel: +44 (0) 7376 625377

16th March 2020

Dear Editor,

Please find enclosed our paper entitled “Application of synchrotron radiation techniques for the characterisation of rare earth element concentration, distribution, crystallography and solid-state chemistry in Nigerian fly ash”, for consideration and inclusion within the journal *Spectrochimica Acta Part B: Atomic Spectroscopy*.

With billions of tons of fly ash already stored in repositories globally, and millions produced annually, extraction of rare earth elements (REEs) from this major untapped resource is urgently required. With Nigeria also turning to coal for electricity generation, such waste material will be present in quantities of many thousands of tonnes, making it a promising source for industrial REE extraction for the country. Understanding the distribution pattern of such REEs within individual micro-mineral particles is therefore essential in the optimisation and development of rare earth extraction methods.

Building on similar papers previously published in this journal (<https://doi.org/10.1016/j.sab.2018.02.009>; [https://doi.org/10.1016/S0584-8547\(01\)00237-3](https://doi.org/10.1016/S0584-8547(01)00237-3); <https://doi.org/10.1016/j.sab.2009.07.032>; [https://doi.org/10.1016/S0584-8547\(02\)00276-8](https://doi.org/10.1016/S0584-8547(02)00276-8)), this paper reports a novel application of synchrotron-based techniques (at the Diamond Light Source) to rare earth mineral particles isolated from bulk fly ash. Our work demonstrates the successful exploration of REE distribution in individual monazite particles, along with speciation (oxidation states) and crystallographic structure transformation. For synchrotron analysis, we used combined micro x-ray fluorescence (μ -XRF) elemental mapping, micro x-ray absorption near edge structure (μ -XANES), μ -XRF tomography and micro x-ray diffraction (μ -XRD).

Novel and first ever characterisation (using synchrotron μ -XRD and μ -XRF tomography) was performed on individual monazite particles to obtain further insight (through 2D and 3D models) into the structural transformation during the coal combustion process and REEs distribution pattern in individual monazite particles. This study has also demonstrated a new analytical technique whereby individual monazite particles are removed from bulk samples using an SEM-mounted micromanipulator (prior to synchrotron radiation analysis), which has been demonstrated as being able to significantly enhance the resolution and quality of the results obtained when compared to

conventional 'bulk' characterisation methods also previously published in this journal (<https://doi.org/10.1016/j.sab.2018.02.009>; <https://doi.org/10.1016/j.sab.2007.01.007>).

The results obtained are essential in underpinning a fundamental understanding of REEs occurrence and distribution in fly ash, for the optimisation of recovery methods and the development of novel techniques to selectively recover these valuable REEs from fly ash (and rare earth ores) while also removing uranium and thorium from the fly ash, thereby making the fly ash safe for recycling into bricks and/or concrete products.

I can attest to the fact that this manuscript (and its figures and tables) are all the sole work of the authors and that we have not submitted this article for consideration elsewhere. We believe that your journal represents the best platform with which to disseminate these time-critical and high-impact results to the most appropriate audience. If you require any further details or clarification on any aspect of this work, please do not hesitate to contact me.

To conclude, we consider that our manuscript fits well within the scope and remit of the Journal *Spectrochimica Acta Part B: Atomic Spectroscopy*. It paves the way for several follow-up publications on novel and low-cost extraction and processing methods for recovering REE from fly ash wastes.

Yours faithfully,

A handwritten signature in purple ink, appearing to read 'Ilemona C. Okeme', is positioned above the printed name.

Ilemona C. Okeme

SAB_2020_128: Reponses to Reviewer

We thank the reviewer for the useful comments and suggestions on the manuscript submitted and we provide the following responses and revisions in line with the comments.

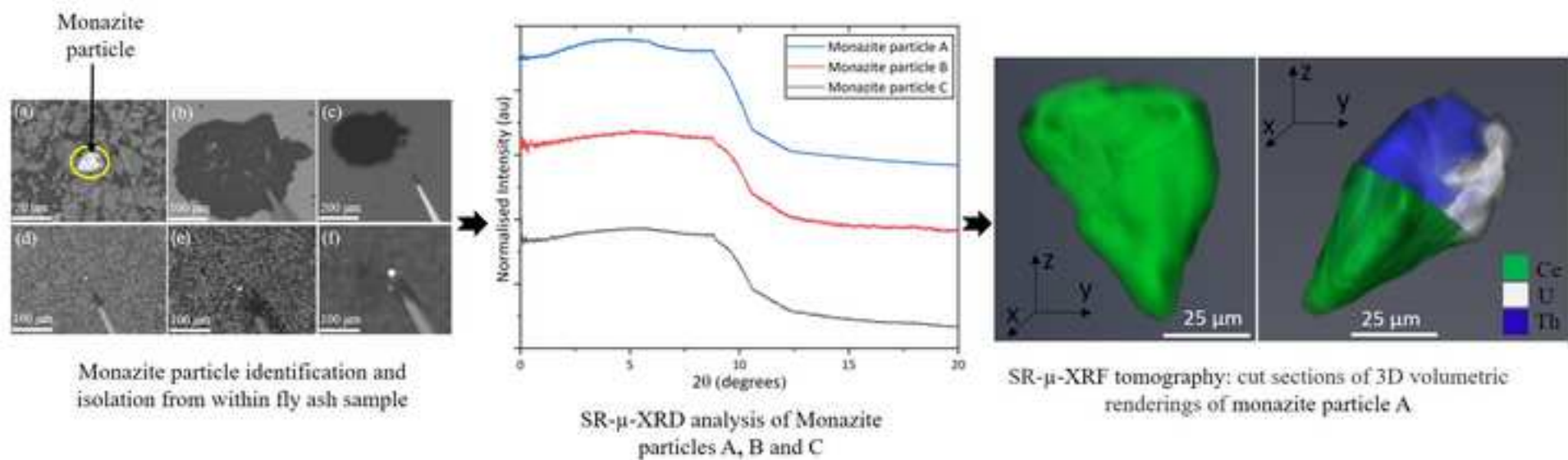
Reviewer 1:

Reference	Comment	Response
1	Definition of u-XRD should be moved to the first occurrence, i.e. from line 111-112 to line 103.	u-XRD has been defined on first use as micro-x-ray diffraction.
2	All over the manuscript: When numbers are written as text, writing by number in brackets is not necessary, e.g. "two (2)" --> "two"	This has been corrected throughout the manuscript.
3	All over the manuscript: Either use weight percent (wt.%) or mass percent (m/m%) but consistently the same.	'wt.%' has been used throughout the manuscript.
4	line 483: "analytical" should be deleted.	'Analytical' has been deleted.
5	Supplementary material: LCF on Ce-L3 XANES would be worth to be presented as a figure (even within Fig.8 of the main manuscript).	LCF on Ce-L3 XANES in the supplementary material has been move into the main manuscript.

Highlights

1
2
3
4
5
6
7
8
9
10
11
12
13
14
15
16
17
18
19
20
21
22
23
24
25
26
27
28
29
30
31
32
33
34
35
36
37
38
39
40
41
42
43
44
45
46
47
48
49
50
51
52
53
54
55
56
57
58
59
60
61
62
63
64
65

- The total rare earth content of the studied samples is promising for recovery.
- Critical rare earths comprised 30wt% of rare earth content within samples studied.
- Micromanipulation method employed to isolate individual monazite particles.
- Radial zonation observed in monazite particles, with rim rich in rare earths.
- Ce oxidised and monazite structure amorphized, increasing chemical reactivity.



25 **Abstract**

26 Fly ash represents a promising alternative source of rare earth elements (REE). However, information
27 on REE containing mineral phases and their association with other fly ash components, vital for REE
28 recovery from fly ash, is currently lacking. Herein, the mass fraction, distribution, crystallography and
29 solid-state chemistry of REE, U and Th in Nigerian simulated fly ash samples were characterised using
30 a range of laboratory and synchrotron x-ray based analytical techniques to underpin future extraction
31 methodologies. Inductively coupled plasma mass spectrometry following full-acid digest of forty-five
32 samples revealed recoverable average total REE content which ranged between 442 mgkg⁻¹ and 625
33 mgkg⁻¹, comprising over 30wt% of the critical REE Nd, Eu, Tb, Dy, Y and Er. These REE within the fly
34 ash samples were found to be most frequently associated with discrete monazite, xenotime and Y-
35 bearing zircon mineral particles, with the former the most detected, which could be
36 beneficiated through gravity separation. Analysis of monazite particles isolated from the composite
37 samples through a complimentary suite of analytical synchrotron radiation techniques revealed a
38 core-shell pattern, with the shell rich in colocalised Ce, Nd and La, and the core enrich in both U and
39 Th. Ce in monazite was found to exist in a mixed trivalent and tetravalent oxidation state, with the
40 monazite structure amorphized due to the high temperature combustion process. Such results
41 demonstrate the strong co-association and physical distribution of REE, U and Th within monazite in
42 fly ash; knowledge of which can subsequently be used to optimise or develop a more selective, cost-
43 effective and environmentally friendly solvent extraction methodology, by targeting the strongly
44 colocalised and surface bound REE in fly ash monazite particles.

45 **Keywords:** Nigeria; fly ash; rare earth elements; monazite; synchrotron radiation.

46 **1. Introduction**

47 Owing to their unique chemical and physical properties, the rare earth elements (REE) are of
48 fundamental industrial importance, with applications including automobiles, green energy, electronics
49 and defence [1,2]. REE consist of chemically similar elements; the fourteen naturally occurring

1
2
3
4
5
6
7
8
9
10
11
12
13
14
15
16
17
18
19
20
21
22
23
24
25
26
27
28
29
30
31
32
33
34
35
36
37
38
39
40
41
42
43
44
45
46
47
48
49
50 lanthanides, plus Y and Sc [3]. Based on their electronic configuration, these elements are further
51 subdivided into the light rare earth elements (LREE) (La to Gd) and the heavy rare earth elements
52 (HREE) (Tb to Lu with Sc and Y) [4]. REE rarely occur in easily exploitable high-grade deposits and never
53 occur as native metals. Their use in final products is therefore dependent upon their efficient
54 extraction from their host minerals [5,6]. When compared against their total average crustal
55 abundance (typically 160 mgkg⁻¹ to 205 mgkg⁻¹ [7]), their mass fraction within minerals and ores is
56 relatively low [3]. Out of the approximately 200 minerals known to contain significant quantities of
57 REE, only bastnaesite ((Ce, La)CO₃F), monazite ((Ce,La,Nd,Th)PO₄), xenotime (YPO₄) and ion-
58 adsorption clays are mined commercially for REE production; with monazite and bastnaesite typically
59 exploited for LREE minerals, and xenotime and ion-adsorption clays for the HREE [8,9]. These REE
60 minerals are accessory minerals of U and Th and are therefore invariably radioactive, constituting a
61 commensurate human health and environmental hazard [9].

62
63
64
65
66
67
68
69
70
71
72
73
74
75
76
77
78
79
80
81
82
83
84
85
86
87
88
89
90
91
92
93
94
95
96
97
98
99
100
101
102
103
104
105
106
107
108
109
110
111
112
113
114
115
116
117
118
119
120
121
122
123
124
125
126
127
128
129
130
131
132
133
134
135
136
137
138
139
140
141
142
143
144
145
146
147
148
149
150
151
152
153
154
155
156
157
158
159
160
161
162
163
164
165
166
167
168
169
170
171
172
173
174
175
176
177
178
179
180
181
182
183
184
185
186
187
188
189
190
191
192
193
194
195
196
197
198
199
200
201
202
203
204
205
206
207
208
209
210
211
212
213
214
215
216
217
218
219
220
221
222
223
224
225
226
227
228
229
230
231
232
233
234
235
236
237
238
239
240
241
242
243
244
245
246
247
248
249
250
251
252
253
254
255
256
257
258
259
260
261
262
263
264
265
266
267
268
269
270
271
272
273
274
275
276
277
278
279
280
281
282
283
284
285
286
287
288
289
290
291
292
293
294
295
296
297
298
299
300
301
302
303
304
305
306
307
308
309
310
311
312
313
314
315
316
317
318
319
320
321
322
323
324
325
326
327
328
329
330
331
332
333
334
335
336
337
338
339
340
341
342
343
344
345
346
347
348
349
350
351
352
353
354
355
356
357
358
359
360
361
362
363
364
365
366
367
368
369
370
371
372
373
374
375
376
377
378
379
380
381
382
383
384
385
386
387
388
389
390
391
392
393
394
395
396
397
398
399
400
401
402
403
404
405
406
407
408
409
410
411
412
413
414
415
416
417
418
419
420
421
422
423
424
425
426
427
428
429
430
431
432
433
434
435
436
437
438
439
440
441
442
443
444
445
446
447
448
449
450
451
452
453
454
455
456
457
458
459
460
461
462
463
464
465
466
467
468
469
470
471
472
473
474
475
476
477
478
479
480
481
482
483
484
485
486
487
488
489
490
491
492
493
494
495
496
497
498
499
500
501
502
503
504
505
506
507
508
509
510
511
512
513
514
515
516
517
518
519
520
521
522
523
524
525
526
527
528
529
530
531
532
533
534
535
536
537
538
539
540
541
542
543
544
545
546
547
548
549
550
551
552
553
554
555
556
557
558
559
560
561
562
563
564
565
566
567
568
569
570
571
572
573
574
575
576
577
578
579
580
581
582
583
584
585
586
587
588
589
590
591
592
593
594
595
596
597
598
599
600
601
602
603
604
605
606
607
608
609
610
611
612
613
614
615
616
617
618
619
620
621
622
623
624
625
626
627
628
629
630
631
632
633
634
635
636
637
638
639
640
641
642
643
644
645
646
647
648
649
650
651
652
653
654
655
656
657
658
659
660
661
662
663
664
665
666
667
668
669
670
671
672
673
674
675
676
677
678
679
680
681
682
683
684
685
686
687
688
689
690
691
692
693
694
695
696
697
698
699
700
701
702
703
704
705
706
707
708
709
710
711
712
713
714
715
716
717
718
719
720
721
722
723
724
725
726
727
728
729
730
731
732
733
734
735
736
737
738
739
740
741
742
743
744
745
746
747
748
749
750
751
752
753
754
755
756
757
758
759
760
761
762
763
764
765
766
767
768
769
770
771
772
773
774
775
776
777
778
779
780
781
782
783
784
785
786
787
788
789
790
791
792
793
794
795
796
797
798
799
800
801
802
803
804
805
806
807
808
809
810
811
812
813
814
815
816
817
818
819
820
821
822
823
824
825
826
827
828
829
830
831
832
833
834
835
836
837
838
839
840
841
842
843
844
845
846
847
848
849
850
851
852
853
854
855
856
857
858
859
860
861
862
863
864
865
866
867
868
869
870
871
872
873
874
875
876
877
878
879
880
881
882
883
884
885
886
887
888
889
890
891
892
893
894
895
896
897
898
899
900
901
902
903
904
905
906
907
908
909
910
911
912
913
914
915
916
917
918
919
920
921
922
923
924
925
926
927
928
929
930
931
932
933
934
935
936
937
938
939
940
941
942
943
944
945
946
947
948
949
950
951
952
953
954
955
956
957
958
959
960
961
962
963
964
965
966
967
968
969
970
971
972
973
974
975
976
977
978
979
980
981
982
983
984
985
986
987
988
989
990
991
992
993
994
995
996
997
998
999
1000

Currently, more than 75% of REE production, nearly half of the known reserves, and the majority of REE metallurgical technologies occur (or are located) in China [2]. Resulting from this near total market monopoly coupled with recent instabilities in the global REE supply market and the projected explosion in demand over the coming decades [2], there is now a renewed incentive for countries to secure economically sustainable REE supply. Amongst this there are a growing number “unconventional sources” such as coal and coal waste products (e.g. coal mine waste, fly ash, acid mine drainage and mine tailings) which have emerged in recent years as highly viable targets for REE recovery [8].

With billions of tons of fly ash already stored in repositories globally, and millions produced annually (especially in the USA, China and India), the development of new methodologies to extract REE from this major untapped resource is urgently required. Following changes in USA-China trading activity in recent years, the USA Senate reintroduced the REE Advanced Coal Technologies Act (REEACT),

1
2 74 initiating research into the development of technologies capable of extracting REEs from coal and coal
3 by-products [10].
4

5 76 The recovery of REEs from fly ash rather than coal and traditional REE-containing ores has several
6 notable advantages [8]. It is a cheap and readily-available post-combustion by-product enriched in
7
8 77 inorganic REE minerals such as phosphates, by a factor of six to ten relative to precursor coal
9
10 78 depending on the geological origin of the feedstock (a consequence of their high melting, boiling, and
11
12 79 thermal decomposition temperatures) [11,12]. Furthermore, fly ash does not require extensive
13
14 80 excavation, unlike the mining of REE ores, which represents a significant capital investment and is
15
16 81 environmentally destructive - REE mining process generates large volumes of waste rock that is rich
17
18 82 in radionuclides. In addition, coal fly ash is an inorganic fine powder, therefore making it ideal for
19
20 83 chemical processing by eliminating the need for costly and energy intensive crushing and grinding.
21
22 84
23
24
25
26

27 85 Previous studies have demonstrated the occurrence and distribution of REE in coal deposits and their
28
29 86 respective ash by-products deposits [13,14]. Seredin et al [14], used inductively coupled plasma-mass
30
31 87 spectrometer (ICP-MS) to characterise coal samples from Russia's Pavlovka coal deposit and found the
32
33 88 REE concentration to be up to 1290 mgkg⁻¹, with the REE in the resulting ash having a mass fraction
34
35 89 (wt%) of 1%. Two further ICP-MS studies of ash samples from a power plant burning coal from the
36
37 90 Kentucky Fire Clay coal bed (a lithology rich in volcanic ash) observed a REE contents of 1200 mgkg⁻¹
38
39 91 to 1670 mgkg⁻¹ [11,12]. Recent surveys published by the United States Department of Energy (US DoE)
40
41 92 indicated total REE contents (not including Sc) of 41 mgkg⁻¹ to 1286 mgkg⁻¹ in U.S. fly ash [15,16].
42
43 93 Additional studies on fly ash using scanning electron microscopy (SEM) coupled with energy dispersive
44
45 94 (x-ray) spectroscopy (EDS), has shown the main REE-bearing phases retained in fly ash to be phosphate
46
47 95 minerals (monazite and xenotime), zircon (ZrSiO₄), bastnaesite, Ce-Nd bearing carbonates, and
48
49 96 organically associated lanthanides [17-19].
50
51
52
53
54
55

56 97 Synchrotron techniques such as micro-x-ray fluorescence (μ -XRF) and micro-x-ray absorption near
57
58 98 edge structure (μ -XANES) have been used extensively to characterise trace metal distribution and
59
60
61
62
63
64
65

99 speciation in different geological materials [20,21]. Within this there have been several studies where
1
2 100 the Ce L_{III} absorption edge in geological materials has been investigated [22,23]. However, while
3
4 101 synchrotron radiation techniques (such as μ -XRF and μ -XANES) have formerly been utilised to examine
5
6 102 the REE composition and distribution within fly ash samples [24,25], other synchrotron radiation
7
8 103 techniques such as μ -XRF tomography and micro-x-ray diffraction (μ -XRD) have not been exploited.
9
10 104 Therefore, studies employing such enhanced synchrotron radiation techniques represent a powerful
11
12 105 means to derive unique information on REEs; such as an elements oxidation state (at the micron scale),
13
14 106 speciation, distribution within REE minerals and alterations to the crystallographic structure, for
15
16 107 combined elucidation of geochemical and thermal changes in the REE minerals within the residual fly
17
18 108 ash following the combustion of the precursor coal.

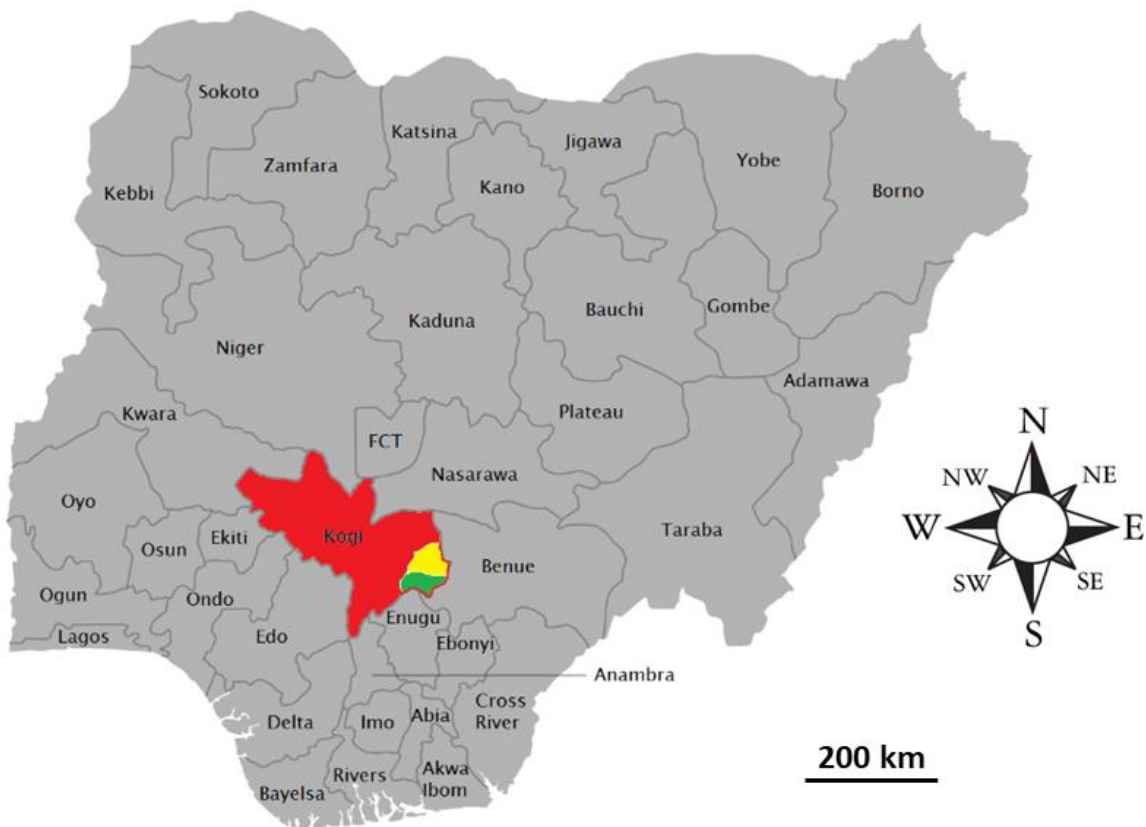
24 109 This study has been established to characterise REE-bearing minerals contained within Nigerian fly ash
25
26 110 samples. To meet this end, single REE-bearing particles within bulk fly ash samples were extracted
27
28 111 from the surrounding matrix prior to synchrotron analysis (μ -XRF and μ -XANES). μ -XRD and μ -XRF
29
30 112 tomography characterisation of such minerals was performed to obtain further insight (through 2D
31
32 113 and 3D models) into the structural transformation that may occur as a result of the combustion
33
34 114 processes, and the REEs distribution pattern within individual monazite micro particles. The results
35
36 115 obtained are essential in developing a fundamental understanding of the distribution and
37
38 116 colocalisation of REE, U and Th within monazite particles, and therefore in the optimisation of recovery
39
40 117 methods for such metals/minerals for both resource recovery and environmental protection [26].
41
42
43
44
45

46 118 **2. Materials and Methods**

49 119 **2.1 Study Area**

52 120 The study examines material sourced from three open-pit coal mines located in Kogi state, Nigeria, as
53
54 121 shown in Figure 1 [27]: both Okaba (OKA) and Odagbo (ODA) mines are located in Okaba and Odagbo,
55
56 122 respectively, within the Ankpa Local Government Area (LGA), with Omelewu (OMA) coal mine located
57
58
59 123 in Imane, within the Olamaboro LGA. The coal mines host sub-bituminous coal (part of the Mamu
60
61
62
63
64
65

124 Formation) and belong to the Kogi mining district, comprising an area of 225 thousand hectare [28,29].
125 Further information on the geologic setting and the coal from these coal mines can be found in [28-
126 32]. Currently, these coal deposits are commercially mined for coal briquette production and as an
127 energy source for nearby cement production [33,34]. Nigeria has known coal reserves of
128 approximately 639 million metric tonnes, with additional estimated reserves of approximately 2750
129 million metric tonnes [35].



130
131 **Figure 1:** Map of Nigerian states showing the location of Ankpa LGA (yellow), and Olamaboro LGA
132 (green) both in Kogi state (red). Modified from [27].

133 2.2 Samples Collection and Preparation

134 Coal samples (each approximately 200 g, packed in polythene bags) were collected from across the
135 three mines using a stratified random sampling method to obtain representative material.

136 Since Nigeria's coal-fired power plants are only at an advanced stage of planning (that is, no
137 operational coal-fired power plants exist in Nigeria from which to obtain fly ash samples), simulant fly

138 ash samples were studied in this work. To simulate fly ash within the laboratory, crushed samples
139 were oven-dried at 100°C for 30 minutes, then pulverised and homogenised before being passed
140 through a 150 µm mesh sieve. The samples were then combusted using a muffle furnace at 1100°C
141 (below the fusion temperature of the ash, while completely removing the organic matter content).
142 This selection of combustion temperature also approximates to the temperature used in coal-fired
143 power plants burning low rank coal (Lignite and sub-bituminous) [36]. The implication of burning low
144 rank coal (at a low temperature) over high rank coal is that it is more likely for the rare earth mineral
145 particles to exist as discretely rather than being encapsulated in the glassy component of ash, since
146 the melting temperatures of glass forming aluminosilicate minerals are higher than this combustion
147 temperature. Following ashing, the samples were left to cool. Sieve analysis revealed that about 80%
148 of these coal ash materials fell in the particle size range of 1 to 300 µm, which translated to 80% fly
149 ash and 20% bottom ash.

2.3 Elemental composition and mineralogical analysis

2.3.1 XRF and XRD analysis

152 To determine the major elements (as oxide ratios) and trace heavy toxic metals in the bulk fly ash
153 samples, a total of 15 fly ash samples per coal mine were analysed using a benchtop Niton™ FXL 950
154 XRF analyser (Ag anode with 50 kV/80 µA maximum X-ray tube, and Si-PIN semiconductor detector).
155 The Niton™ FXL 950 XRF analyser is self-calibrating – running on a factory installed calibration
156 software (called ‘Fundamental Parameter’ (FP)), to accurately measure elemental concentrations and
157 automatically correct for matrix and inter-element effects. Prior to samples analysis, the calibration
158 of the analyser was further checked and confirmed not to have drifted by running two reference
159 materials (USGS SdAR-M2 and NIST 2709a). The pulverised, homogenised and sieved fly ash samples
160 (Section 2.2) were each packaged into XRF sample cups and scanned for two (2) minutes (live time);
161 to ensure an accurate reading and increased sensitivity. Normalisation and quantification of the
162 results were performed using the Thermo Scientific Inc. NDT™ package.

163 Mineralogical analysis of the fly ash samples was performed on composite OMA, OKA and ODA bulk
164 fly ash samples using a Philips X'pert™ diffractometer system with a Cu anode operated at a voltage
165 and current of 40 kV and 30 mA, respectively. The scans were run from 10 to 80 degrees 2θ, with
166 increments of 0.07 degrees at a counting time of 10 seconds per step. The minerals phases were then
167 determined and quantified using the match™ phase identification package.

168 **2.3.2 ICP-MS analysis of REE**

169 The REE mass fraction of each fly ash sample was analysed using total acid digestion followed by ICP-
170 MS using the method of Garbe-Schönberg [37]. A total of 45 fly ash samples (15 per coal mine) were
171 prepared for analysis. The samples were first homogenised by gentle agitation and 100 mg was
172 transferred into individual 50 mL screw cap teflon digestion vessels. 4mL of HF (47-51% Trace metal
173 grade; Fisher Scientific) followed by 3 mL of HCl (34-37% Trace metal grade; Fisher Scientific) and then
174 1 mL of HNO₃ (67-69% Trace metal grade; Fisher Scientific) was then added to each sample using a
175 micropipette. Time was allowed between each step to allow any reactions to subside. The reaction
176 vessels were then sealed, and each placed in DigiPrep digestion blocks (preheated to 160°C) for 18
177 hours. The vessels were then removed from the DigiPrep system and allowed to cool to room
178 temperature. 1 mL of HClO₄ (65% Normatom; VWR™) was then added to each sample which were
179 then returned to the DigiPrep system and heated to 180°C until incipient dryness.

180 Samples were then removed from the DigiPrep system and allowed to cool to room temperature. This
181 step was then repeated but using 1 mL HNO₃ (67-69% Trace metal grade; Fisher Scientific). 1 mL of
182 conc. HNO₃ (67-69% Trace metal grade; Fisher Scientific) and 5 mL of deionised water were then added
183 to each sample which were returned to the DigiPrep system and heated to 100°C for 30 minutes.
184 Samples were then removed from the DigiPrep system and allowed to cool to room temperature. 44
185 mL of deionised water were then added to each sample.

186 Samples were then prepared for ICP-MS analysis by diluting 5 mL aliquots using 45 mL of 5% HNO₃.
187 (67-69% Trace metal grade; Fisher Scientific). Measurements was performed using an Agilent 7700x.
188 Duplicates, blanks and replicates of a Reference Material (USGS: AGV-1 and DNC-1) were ran for every
189 10 samples. Calibration was performed using a Inorganic ventures ICP-71A multi-elemental ICP-MS
190 calibration standard.

191 **2.4 SEM-EDS REE Particle Location**

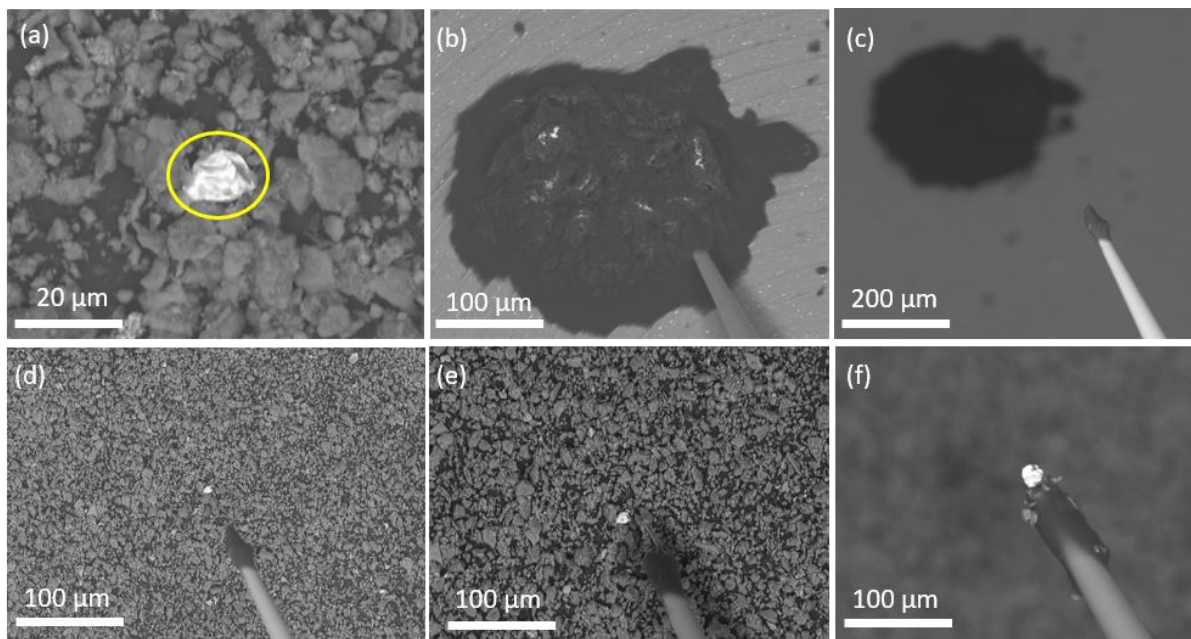
192 Representative composite OMA, OKA and ODA bulk ash samples for initial analysis within the SEM
193 were prepared by depositing a fine layer of fly ash (<1 g) on to a 12 mm low elemental background
194 adhesive carbon (Leit) disc mounted on a standard SEM pin-stub. The samples were then examined
195 using a Zeiss SIGMA™ Field Emission SEM fitted with secondary electron (Everhart Thornley SE2) and
196 backscattered electron (AsB) detectors using the instrument's Variable Pressure (VP) mode to negate
197 against the requirement for a conductive coating while preventing surface charging. Using the
198 backscattered electron detector (AsB), mineral particles containing trace levels of high atomic (Z)
199 number elements in the samples (e.g. REE minerals) appeared as bright (white) spots against the
200 otherwise dark sample background. REE mineral particles were then identified based on their
201 characteristic elemental composition following confirmatory EDS analysis. The elemental composition
202 and subsequently the mass fraction (wt% ± percentage error, δ) were determined using an EDAX™
203 Octane Plus high-resolution EDS system comprising an electronically cooled Silicon Drift Detector
204 (SDD). At a voltage of 30 keV, aperture of 120 μ m (in high current mode) and acquisition time of 200
205 second, the whole surface of each identified REE mineral particle was raster scanned, and data analysis
206 undertaken using the associated EDAX (AMETEK Inc.) TEAM™ software.

207 **2.5 REE Particle Isolation**

208 Following the particles prior identification, in-situ removal of the identified micron-scale REE-bearing
209 monazite particles from the bulk samples was performed within the SEM using an MM3A-EM
210 Micromanipulator from Kleindiek Nanotechnik [38]. This piezo-electric device, capable of stepwise

211 vertical, retractive, rotational and lateral motion at minimum incremental movements of 1 nm was
212 used to control an extruded glass capillary with a tip diameter of approximately 1 μm . To negate
213 against the effects of electron beam induced charging, the non-conductive extruded glass capillary
214 was coated with approximately 2 nm of sputter-deposited gold.

215 The lift-out process reported in Martin et al [39] for uranium particles was used in this work to extract
216 the REE containing monazite particles – similarly utilising the electron-beam hardening adhesive
217 SEMGlu™, also by Kleindiek [40]. A schematic of the isolation process is detailed in Figure 2. Following
218 their SEM-EDS characterisation, each monazite particle extracted from the bulk fly ash (still adhered
219 to the glass capillary needle) was securely enclosed in Kapton™ tape in preparation for subsequent
220 synchrotron radiation analysis. Owing to the morphological and compositional similarities of the suite
221 of monazite particles identified in the composite OKA, ODA and OMA fly ash samples, only three (3)
222 monazite particles were prepared in this way for synchrotron analysis.



223
224 **Figure 2:** In-situ REE particle isolation process performed within the Zeiss SIGMA VP SEM using the
225 Kleindiek MM3A Micromanipulator. (a) locating particle using backscattered electron detector and
226 co-incident EDS; (b) and (c) applying small quantity of the electron-beam hardening SEMGlu™ to the
227 extruded tip of glass capillary; (d) and (e) progressively lowering the glass capillary to approach the
228 particle (f) removing the particle from the surrounding bulk material, attached to the capillary tip.

229 2.6 Synchrotron Radiation Analysis

1
2
3 230 Synchrotron μ -XRF, μ -XRF tomography, μ -XANES and μ -XRD analyses were performed at Diamond
4
5 231 Light Source on the micro-focus spectroscopy beamline (I18). Diamond is a medium-energy third
6
7 232 generation synchrotron with the storage ring operated at 3 GeV and nominal beam current of 300 mA.
8
9
10 233 The I18 beamline, with an energy range of 2.05 keV and 20.5 keV, is equipped with a cryogenically
11
12 234 cooled double crystal Si[111] monochromator (for energy tuning) and Kirkpatrick–Baez (KB) mirrors
13
14 235 for the focusing of the beam (to a spot of $2\ \mu\text{m} \times 2\ \mu\text{m}$) onto the sample, and harmonic rejection. The
15
16 236 beamline was equipped with a Vortex-ME4TM multi-element Silicon drift fluorescence detector (SDD)
17
18
19 237 and a high-resolution X-ray scientific Complementary Metal–Oxide–Semiconductor (sCMOS) camera
20
21 238 for μ -XRF, μ -XRF tomography, μ -XANES and μ -XRD data acquisition, respectively. To prevent detector
22
23 239 saturation, a 0.1 mm Al foil was inserted. Further details of the optical and detector setup of the I18
24
25 240 beamline can be found in Mosselmans et al [41]. Throughout all sample analyses, a consistent beam,
26
27 241 sample and detector geometry were maintained.
28
29
30

31 32 2.6.1 μ -XRF

33
34
35 243 Each particle was mounted on a kinematic stage at 45° to the incident beam, with the fluorescence
36
37 244 detector oriented at 90° (perpendicular) to the incident beam. Each particle was raster-scanned
38
39 245 through the beam at an energy of 18 keV (above the L_{III} edge energies of Ce (5723 eV), Nd (6208 eV),
40
41 246 La (5483 eV), U (17166 eV) and Th (16300 eV)) using a step size of $2.5\ \mu\text{m}$, and dwell-time of 30 second
42
43 247 per step. Resulting from the comparably thin sample thickness, elemental composition data was
44
45 248 acquired in fluorescence mode using the Vortex-ME4TM multi-element Silicon drift fluorescence
46
47 249 detector (SDD) – fitted using PyMCA and visualised in 2D using Diamond’s in-house DAWN software
48
49
50 250 [42].
51
52
53
54
55 251
56
57
58 252
59
60
61
62
63
64
65

253 2.6.2 μ -XRF tomography

1
2
3 254 The μ -XRF technique provides a depth averaged 2D representation of a 3D distribution of elements,
4
5 255 hence does not reveal 3D information on the location of elements on the surface or within a particle.
6
7
8 256 This limitation is resolved through μ -XRF tomography technique. μ -XRF tomography analysis was
9
10 257 performed on monazite particle **A**, to obtain 3D information on REE, U and Th distribution in the
11
12 258 particle. For each fluorescence tomographic scan, the particle was raster scanned while progressively
13
14 259 being translated through the beam (using a step size of 2.5 μm), and then rotated through 180° with
15
16 260 constant angular steps of 3°, at a dwell-time of 60 millisecond. Fluorescence projections were acquired
17
18 261 using a sCMOS x-ray camera coupled with a gadolinium oxysulphide scintillator screen. Corrections
19
20 262 for absorption within the particle matrix and reconstruction of the fluorescence projections collected
21
22 263 was completed using iterative algorithms, with a 3D volumetric rendering of the particle performed
23
24 264 using the FEI Avizo™ software [43].
25
26
27
28
29

30 2.6.3 μ -XANES

31
32
33 266 Following the μ -XRF analyses, μ -XANES data were acquired (at respective L_{III} edge energy) for Ce
34
35 267 (5723 eV), Nd (6208 eV) and La (5483 eV) at spots identified as containing high concentrations of
36
37 268 these elements within each monazite particle. For each of Ce, La and Nd, in the pre and post edge
38
39 269 regions, energy steps of 0.25 eV were used, with steps of 0.1 eV used across the main edge region using
40
41 270 a dwell-time of 30 seconds per step. μ -XANES data were processed (calibrated against respective Ce,
42
43 271 La and Nd L_{III} edge energies, deglitched, normalised and fitted) using the ATHENA software suite
44
45 272 [44]. The quantification of Ce (III) and Ce (IV) in the normalised $\mu(E)$ Ce μ -XANES spectrum was
46
47 273 undertaken in ATHENA by linear combination fitting (LCF), using a fit range of -30 eV to 70 eV
48
49 274 around the Ce L_{III} edge. The weights of the reference compounds were forced to be between 0 and 1
50
51 275 with no restriction on the edge energy, E_0 .
52
53
54
55
56
57
58
59
60
61
62
63
64
65

278 2.6.4 μ -XRD

1
2
3 279 For μ -XRD, the sCMOS camera was aligned directly downstream of the sample along the path of the
4
5 280 beam of energy, 18 keV. The sample was rotated through 180° during exposure and data acquired in
6
7 281 transmission mode. Data processing (background correction, 2D and 1D visualisations) of the
8
9
10 282 diffraction patterns were additionally performed using the DAWN software.

13 3. Results and Discussion

16 284 3.1 XRF and XRD analysis

17
18
19
20 285 Table S1 (Appendix) and Figs. S1, S2, and S3 (Appendix) show the XRF and XRD results for OMA, OKA
21
22 286 and ODA fly ash samples. The average XRF results (in wt%) showed that the fly ash samples are largely
23
24 287 composed of SiO₂ (>54%) and Al₂O₃ (>19%), alongside 2% to 7% Fe₂O₃, TiO₂ and CaO (except for OMA
25
26 288 samples with CaO level of less than 1%). In OMA, OKA and ODA samples, the sum of SiO₂, Al₂O₃ and
27
28 289 Fe₂O₃ were greater than 70% with CaO level also less than 8%; this implies OMA, OKA and ODA fly ash
29
30
31
32 290 classify as class F according to the ASTM standard [45]. Previous study has shown that high calcium
33
34 291 concentration (as in the case of OKA and ODA) is associated with extractability of REE associated with
35
36 292 calcium-bearing phases in the fly ash, due to the high solubility of the calcium-bearing phases in nitric
37
38
39 293 acid [46]. Results from previous proximate analysis carried out on OMA, OKA and ODA fly ash samples
40
41 294 by Afu et al., Mohammed et al. and Chukwu et al. [30-32] (table S2 (Appendix)) shows that OMA, OKA
42
43 295 and ODA fly ash have ash content (in wt%) of 14.8%, 10.7% and 5.3%, respectively. This result agrees
44
45 296 with studies on fly ash sourced from coal-fired power plants [24,47]. Although occurring as few to
46
47 297 hundreds of mgkg⁻¹ relative to the large volume of fly ash that would be generated annually, the trace
48
49
50 298 toxic heavy metals (Pb, As, and Cr) are of serious environmental concern and capital intensive during
51
52 299 rare earth extraction.

53
54
55
56 300 The results (in wt%) from XRD analysis showed quartz (SiO₂) and mullite (3Al₂O₃.2SiO₂) as the major
57
58 301 mineral phase alongside trace amount (of less than 1%) of hematite and cristobalite (polymorph of
59
60
61
62
63
64
65

1
2 302 quartz formed during the high temperature combustion process). These results also agree with the
3 303 XRD studies on fly ash samples from coal-fired power plants [15,47].
4

5 304 **3.2 ICP-MS analysis of REE and economic valuation**

6
7
8 305 Shown in Tables S3, S4 and S5 (Appendix), respectively, are the complete results of REE measurement
9
10 306 with ICP-MS for OMA, OKA and ODA fly ash samples. The samples were highly concentrated in the
11
12 307 LREE, with Ce followed by Nd the most abundant LREE in all samples. Of the HREE, Y, Sc, Gd and Dy
13
14 308 were the most abundant, with Eu, Tb, Ho, Tm and Lu being just a few mgkg^{-1} (characteristic of non-
15
16 309 ore HREE sources), indicating low occurrence of HREE minerals in the studied fly ash samples. This
17
18 310 abundance pattern of the light and the heavy REE in the fly ash samples conforms to the Oddo-Harkins
19
20 311 Rule, where in this case, the REE with even atomic number (Z) are more abundant than the ones with
21
22 312 odd Z.
23
24
25
26

27
28 313 As shown in Table 1, the mean total REE (plus Y and Sc) for OMA, OKA and ODA were 623 mgkg^{-1} , 442
29
30 314 mgkg^{-1} and 441 mgkg^{-1} respectively, with the fraction of the critical REE (Nd, Eu, Tb, Dy, Y and Er) being
31
32 315 37%, 30% and 28%, respectively. When compared with the Upper Continental Crust Abundance (UCCA)
33
34 316 as in Tables S3, S4 and S5 (Appendix), the total REE content were 2 to 4 times enriched in the fly ash
35
36 317 samples (with Ce being 6 times enriched in the OMA fly ash). Though these concentrations were
37
38 318 generally well below concentrations in conventional REE ores [3], the large volume fly ash generated
39
40 319 annually in addition to little or no extra cost of ore mining and waste rock handling is a significant
41
42 320 advantage. These results are comparable with results of previous studies on USA, Chinese and Indian
43
44 321 fly ash samples (Table 1).
45
46
47
48
49

50 322

51
52
53 323

54
55
56 324

57
58
59 325
60
61
62
63
64
65

Table 1: Comparison of mass concentration (mgkg^{-1}) of total REE (TREE) in fly ash with those of top coal consuming countries.

Coal source	TREE	Critical REE (%)	Reference
Omelewu coal, Nigeria	623	37	This study
Okaba coal, Nigeria	442	30	This study
Odagbo coal, Nigeria	441	28	This study
Jungar, Inner Mongolia, China	293.5	28.3	Dai et al., 2014b [48]
Bhusawal coal plant (unspecified mine), India	384.1	26.3	Modal et al., 2019 [49]
Central Appalachian (Fire Clay), USA	1667.6	36.5	Mardon and Hower, 2004 [50]
Central Appalachian, USA	401.5	38.6	Hower et al., 2013b [51]
Illinois Basin, USA	312.1	36.2	Hower et al., 2013b [51]
Central Appalachian, USA	563.6	38.1	Hower et al., 2013b [51]
Powder River Basin, USA	283.2	32.8	Taggart et al., 2016 [52]

3.2.1 Economic valuation of REE content of fly ash

Table S6 (Appendix) shows the REE mass fractions expressed as rare earth oxide (REO), with OMA REO mean value slightly higher than that of Round Top Mountain—a rhyolite laccolith intrusion enriched in Y and other HREE [53]. On REO basis, the economic valuation shows that these fly ash samples have very strong potential of recovering REO worth millions of dollars. Using the ash content values of OMA, OKA and ODA fly ash samples (14.8%, 10.7% and 5.3%, respectively), (Table S2 (Appendix)), and an initial projected annual consumption of 27 million metric tonnes of coal by the proposed coal-plants [28], this amounts to 1330 thousand, 960 thousand and 480 thousand metric tonnes of fly ash generated annually from OMA, OKA and ODA coal mines, respectively (assuming equal supply of coal

1 355 from all mines). Using the REO values (Table S6 (Appendix)), we estimated that a total of 1752
2 356 tonnes/year (1 751 844.7 kg/year) of REO is recoverable from Nigerian fly ash, translating into annual
3
4 357 value of \$41 204 000 dollars (Table S7 (Appendix)). Though this economic valuation does not include
5
6
7 358 costs of recovery (with cost-effective technologies currently under development), it provides the basis
8
9 359 for evaluating viability of REE extraction from fly ash. One major advantage of using fly ash as
10
11 360 alternative source of REE is the minimal expense associated with the mining processes, such as
12
13 361 blasting, prospecting, and transport. The measurement results also show that the potential value of
14
15 362 REE in fly ash is dependent on REE class (LREE vs HREE), with the high prices of Sc, Nd and the HREE,
16
17 363 contributing considerably to the REE value in fly ash.
18
19
20
21

22 364 **3.3 SEM-EDS**

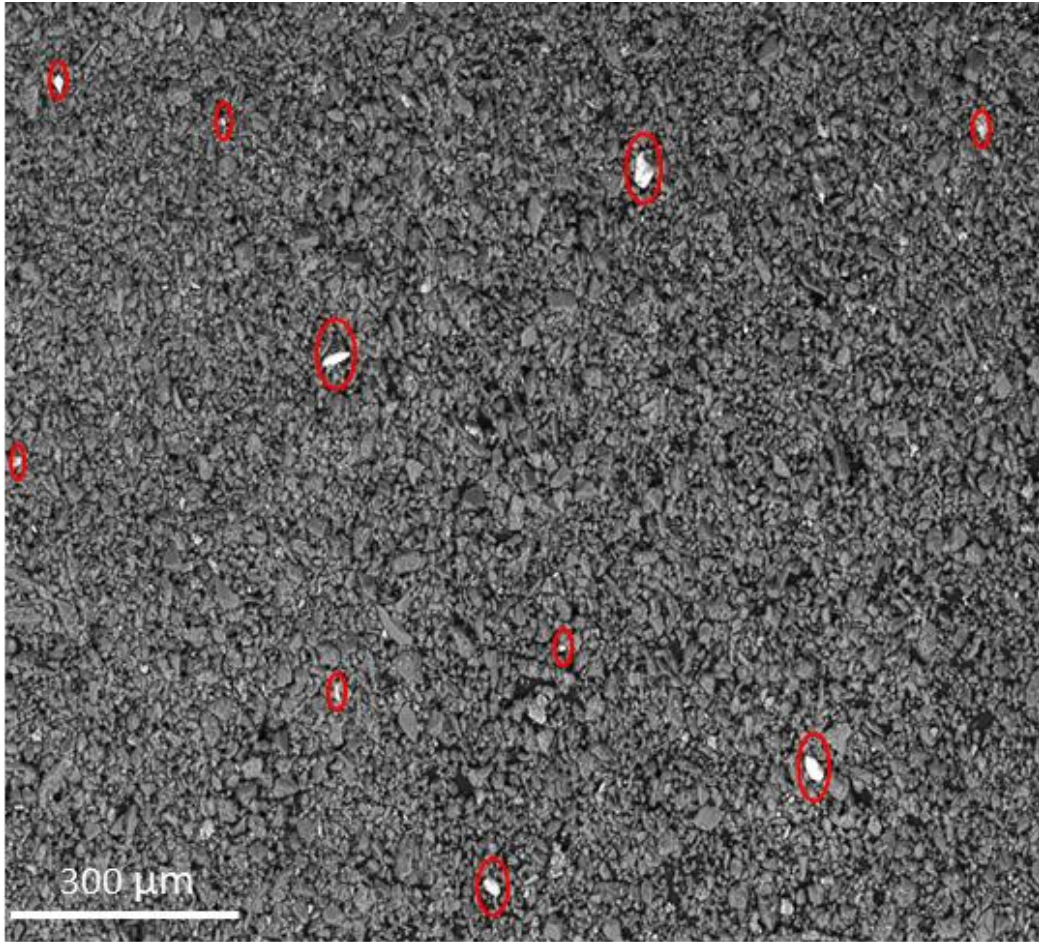
23
24
25 365 Fig. 3a is an SEM image showing the distribution and abundance of REE minerals in a fly ash sample.
26
27 366 Fig. 3b shows the SEM image and EDS spectra of three monazite particles **A**, **B** and **C**, respectively.
28
29 367 Also, the mass fraction (wt% \pm percentage error, δ) elemental composition of ten (10) monazite
30
31 368 particles identified within composite OMA, OKA and ODA samples, respectively, is shown in Table S8
32
33 369 (Appendix). These are typical of the suite of monazite particles found in the fly ash samples studied.
34
35 370 From the SEM-EDS results, trace monazite particles were the predominant REE mineral within the fly
36
37 371 ash samples, alongside scanty xenotime and Y-bearing zircon particles (Figs. S4a and S4b (Appendix)
38
39 372 and Table S9 (Appendix)). This confirms the ICP-MS result which recorded highest concentration for
40
41 373 Ce and Y. As can be seen in Fig. 3b and table S8 (Appendix), the detected monazite particles were the
42
43 374 same in composition and morphology, with weathered surfaces characteristic of monazite of detrital
44
45 375 origin. Strong Al and Si peaks signified the occurrence of quartz and mullite, the major mineral phases
46
47 376 in fly ash [24]. The monazite particles are ascribed to a detrital source, transported by water or wind
48
49 377 from a nearby granitic highland, deposited and subsequently incorporated into the coal during
50
51 378 coalification [18]. These REE minerals (between 10 μ m and 80 μ m in size) were found to exist largely
52
53 379 as discrete particles and not encapsulated in glassy phases, making the extraction and isolation of
54
55
56
57
58
59
60
61
62
63
64
65

1 380 these discrete particles more cost-effective, as leaching rare earth mineral particles encapsulated in
2 381 glassy phases consumes more costly reagents and generates significant volumes of waste products. Y
3
4 382 though abundant in the fly ash materials, its extraction will be difficult since its host mineral (zircon)
5
6
7 383 is a refractory mineral. Studies have shown that REE mineral particles become encapsulated in quartz
8
9 384 and mullite mineral particles during coal combustion process, mainly during the combustion of high
10
11 385 rank coal at temperatures between 1500°C and 1700°C) [46,47]. Hence, combustion of low rank coal
12
13 386 at temperatures between 900°C and 1200°C greatly reduces sequestration of REE minerals into
14
15 387 aluminosilicate glass phases, making REE extraction from fly ash cost effective. Our results agreed with
16
17 388 previous studies on fly ash (sourced from coal-fired plants burning high rank coal) that REE mineral
18
19 389 particles were either dispersed throughout the glass phase, or as independent particles outside of
20
21 390 glass [17].
22
23
24
25
26
27
28
29
30
31
32
33
34
35
36
37
38
39
40
41
42
43
44
45
46
47
48
49
50
51
52
53
54
55
56
57
58
59
60
61
62
63
64
65

391

392

1
2
3
4
5
6
7
8
9
10
11
12
13
14
15
16
17
18
19
20
21
22
23
24
25
26
27
28
29
30
31
32
33
34
35
36
37
38
39
40
41
42
43
44
45
46
47
48
49
50
51
52
53
54
55
56
57
58
59
60
61
62
63
64
65



393

394

395

Fig. 3a: Backscattered electrons image showing distribution and abundance of micro REE mineral particles in a fly ash sample, with the particles appearing white in contrast to the surrounding material.

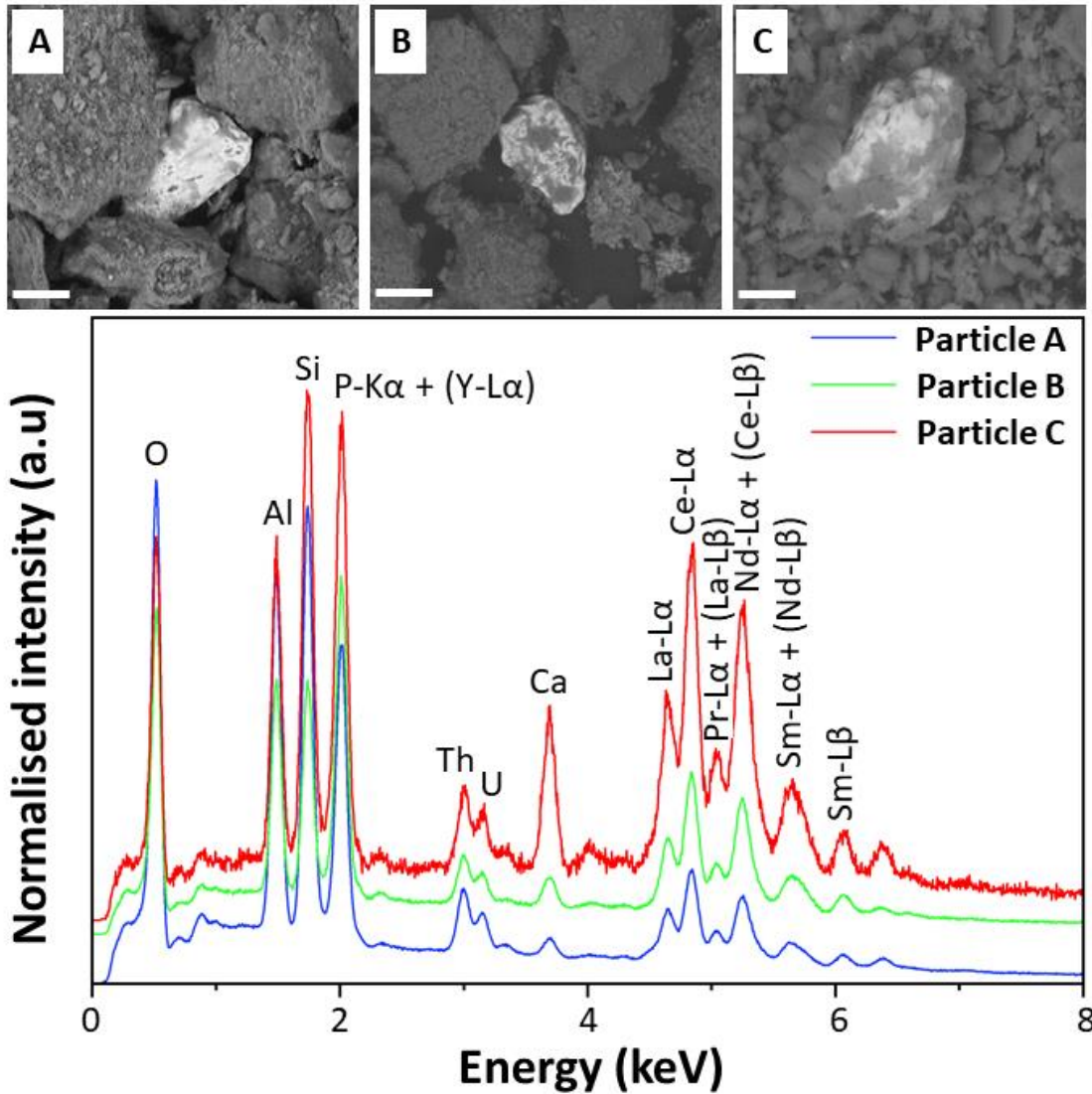


Fig. 3b: (top) Electron microscope images of monazite particles (A, B and C) alongside, (bottom) the associated EDS spectra, with emission peaks identified. (Scale bars = 50 μm).

3.4 $\mu\text{-XRF}$

Fig. 4 shows the elemental composition maps of monazite particles A, B and C. From the results, the monazite particles show a core-shell pattern, with the shell rich in strongly colocalised Ce, La and Nd, and a Th and U rich core. U and Th were both observed to colocalise strongly, however, both poorly with the LREE. The chemical similarities (such as atomic radius) account for this observed colocalisation of the LREE [54]. The core-shell zonation of the actinides and LREE in the monazite particles is characteristic of detrital monazite, formed during magmatic growth or recrystallisation of the monazite particles [55].

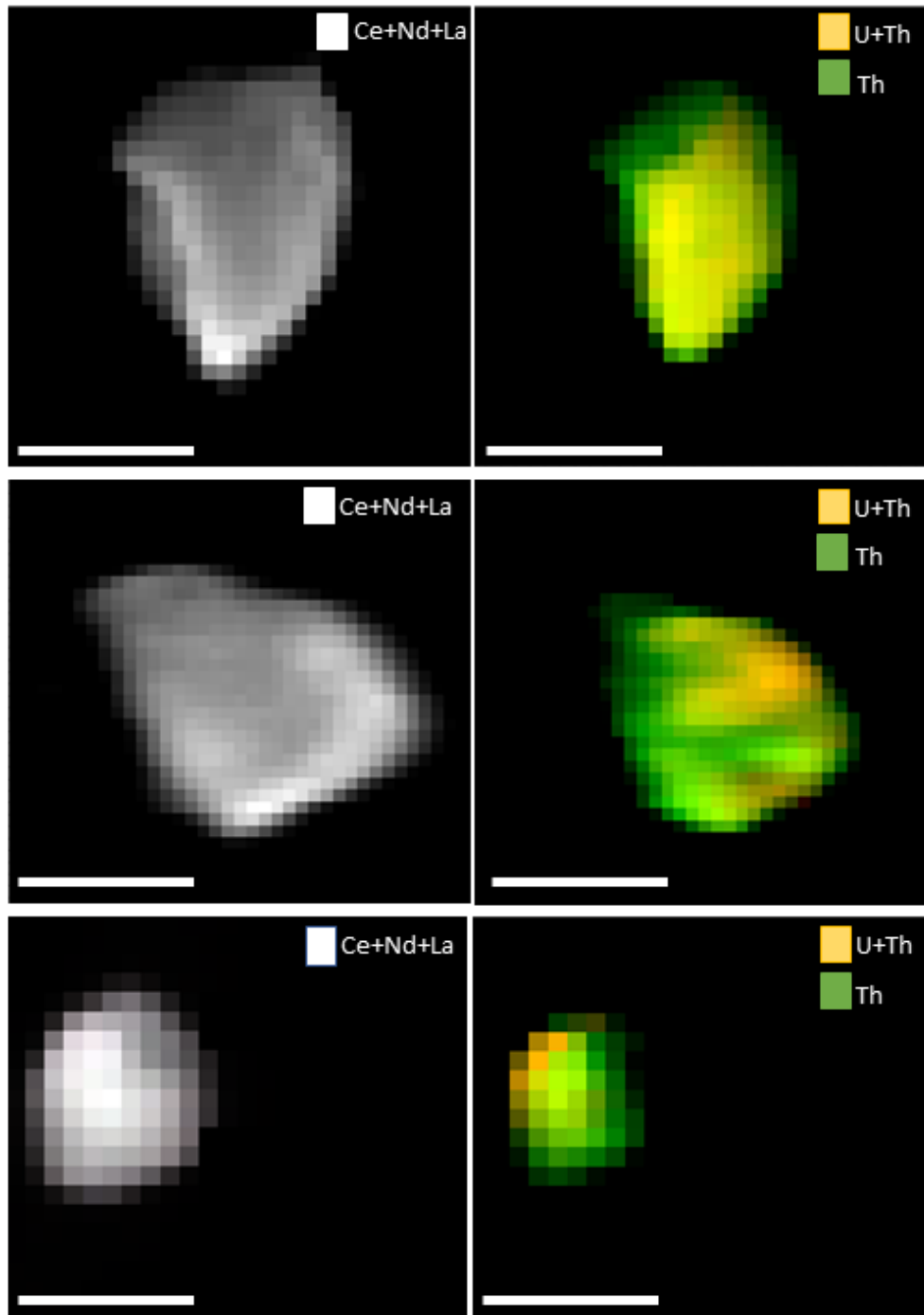
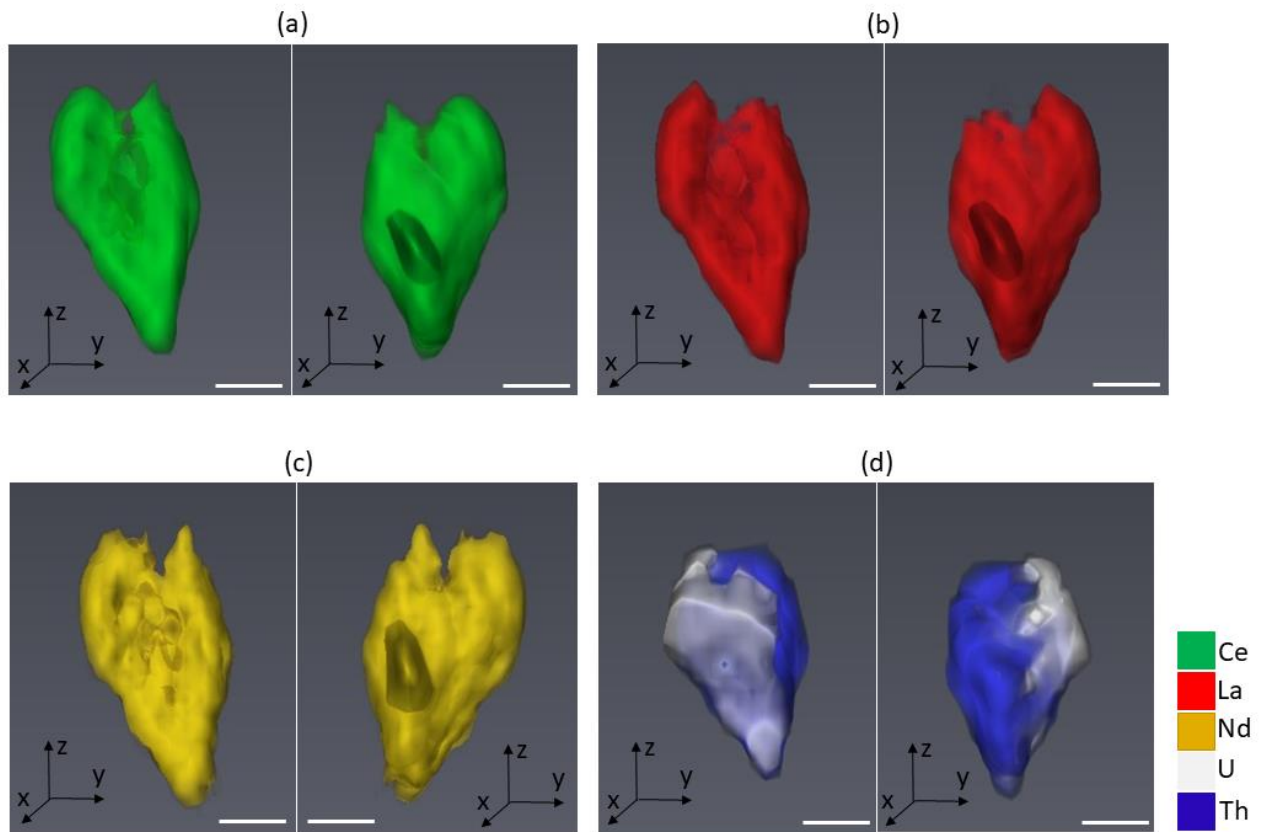


Fig. 4: μ -XRF maps (Ce, Nd, La, U and Th) of monazite particles **A**, **B** and **C**, illustrating the compositional variance of these elements (scale bars = 50 μ m).

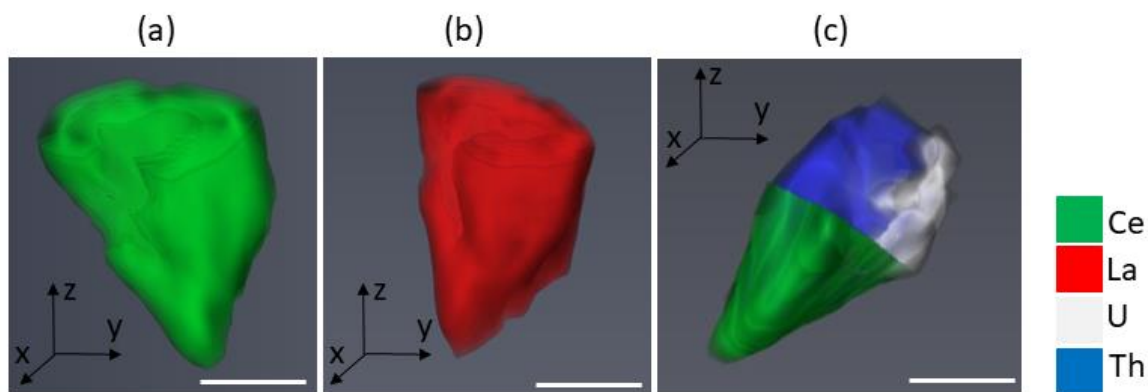
3.5 μ -XRF tomography

Renderings of the μ -XRF tomography data on monazite particle **A** are shown in Figs. 5, 6 and 7. The results highlight the core-shell distribution of elements within the particle (Fig. 6), with the REE Ce, La and Nd confirmed to be surface bound, surrounding Th and U (Figs. 6 and 7). Both Th and U were

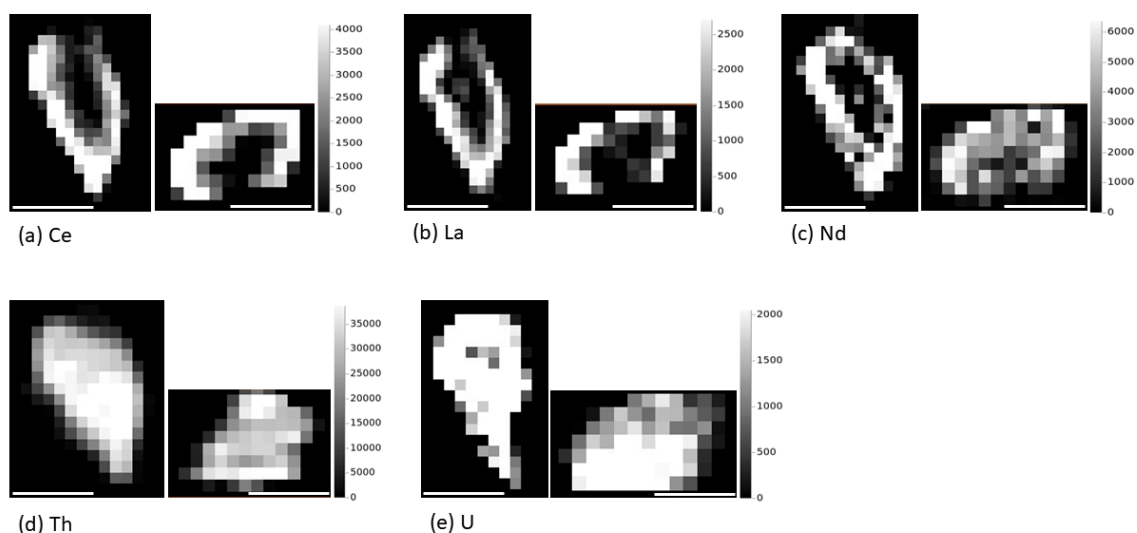
414 observed to exist as strongly colocalised in the core of the monazite particle, while being
415 simultaneously depleted around its shell [Figs. 6 and 7], confirming the earlier μ -XRF results. Being
416 surface bound, these REE would have the potential to be preferentially leached during an extraction
417 process (compared to U and Th, that are conversely located within the particle centre). This finding is
418 significant in the development of a selective extraction methodology, targeting the strongly
419 colocalised and surface bound REE in fly ash monazite particles. The μ -XRF tomography results have
420 also illustrated that the monazite particle is of high density and is also non-porous; implying that the
421 surface pits (identified by the SEM imaging) do not permeate significantly into the underlying monazite
422 structure.



423
424 **Fig. 5:** 3D volumetric rendering (Front and back views) of Ce, La, Nd, U and Th in monazite
425 particle **A**. Scale bars = 25 μ m.



428
429 **Fig. 6:** Cut sections of 3D volumetric renderings of monazite particle **A** showing the core-shell pattern.
430 (a) and (b): hollow interior within Ce and La volumetric renderings. (c): Ce outer shell with U and Th
431 components within the core. Scale bars = 25 μm .



432
433 **Fig. 7:** Greyscale plots in the xy and xz planes (arbitrary units) showing monazite particle **A** with a REE
434 rich rim and a REE depleted core. Scale bars = 25 μm .

435 3.6 μ -XANES

436 The μ -XANES spectrum across the Ce, La and Nd L_{III} -edge in monazite particles **A**, **B** and **C**, alongside
437 their reference standards [57], are shown in Figs. 8a-8c. from Fig. 8a, the Ce (III) reference has a single
438 peak at *P* (5727.5 eV) with the peaks at *Q* (5731 eV) and *R* (5738 eV) representing the Ce (IV) reference.
439 The μ -XANES spectrum of Ce in particle **A** (Fig. 8a) displays two peaks-an intense peak at 5727.5 eV
440 (position *P*), corresponding to Ce (III), and a subtle peak at 5738 eV (position *R*), corresponding to Ce
441 (IV) minor contribution. This invokes a micro-scale oxidation of Ce (transitioning from III to IV) resulting

1
2
3
4
5
6
7
8
9
10
11
12
13
14
15
16
17
18
19
20
21
22
23
24
25
26
27
28
29
30
31
32
33
34
35
36
37
38
39
40
41
42
43
44
45
46
47
48
49
50
51
52
53
54
55
56
57
58
59
60
61
62
63
64
65

442 from the thermal decomposition of the detrital monazite particles, during the high temperature
443 combustion process and illustrates that Ce existed in mixed oxidation states of III and IV. Ce (III) has
444 the tendency to lose an electron to become $4f^0$, and hence form the stable Ce (IV) [54]. LCF using Ce
445 (III) ($CeTiO_3$) and Ce (IV) (CeO_2) references revealed a Ce (III) and Ce (IV) ratio of 80%:20% (Table 2),
446 which affirms a micro scale oxidation due to the high temperature combustion process. These results
447 agree with an earlier work, noting possible processing differences [24].

448 Both La and Nd in particles **A**, **B** and **C** (Figs. 8b and 8c) were found to exist only in the III oxidation
449 state, with distinct peak at 5485 eV and 6214 eV, respectively. This result coupled with the existence
450 of similarity in the pre- and post-edge features between the particles and reference La and Nd spectra,
451 suggest that the La and Nd chemistry for the particles is unaffected by the high temperature
452 combustion process and resistant to oxidation. The similarity in chemical properties of the REE
453 explains the prevalence of the 3+ oxidation state.

454

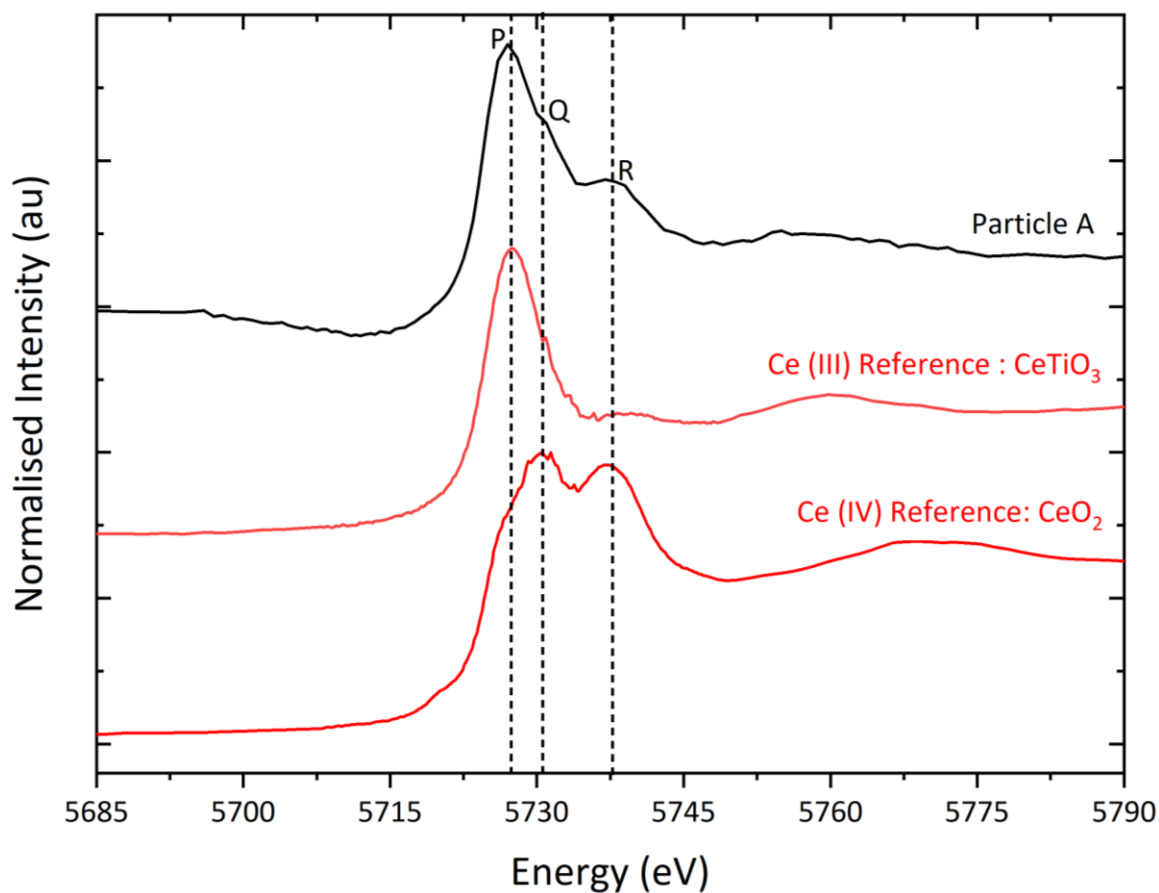
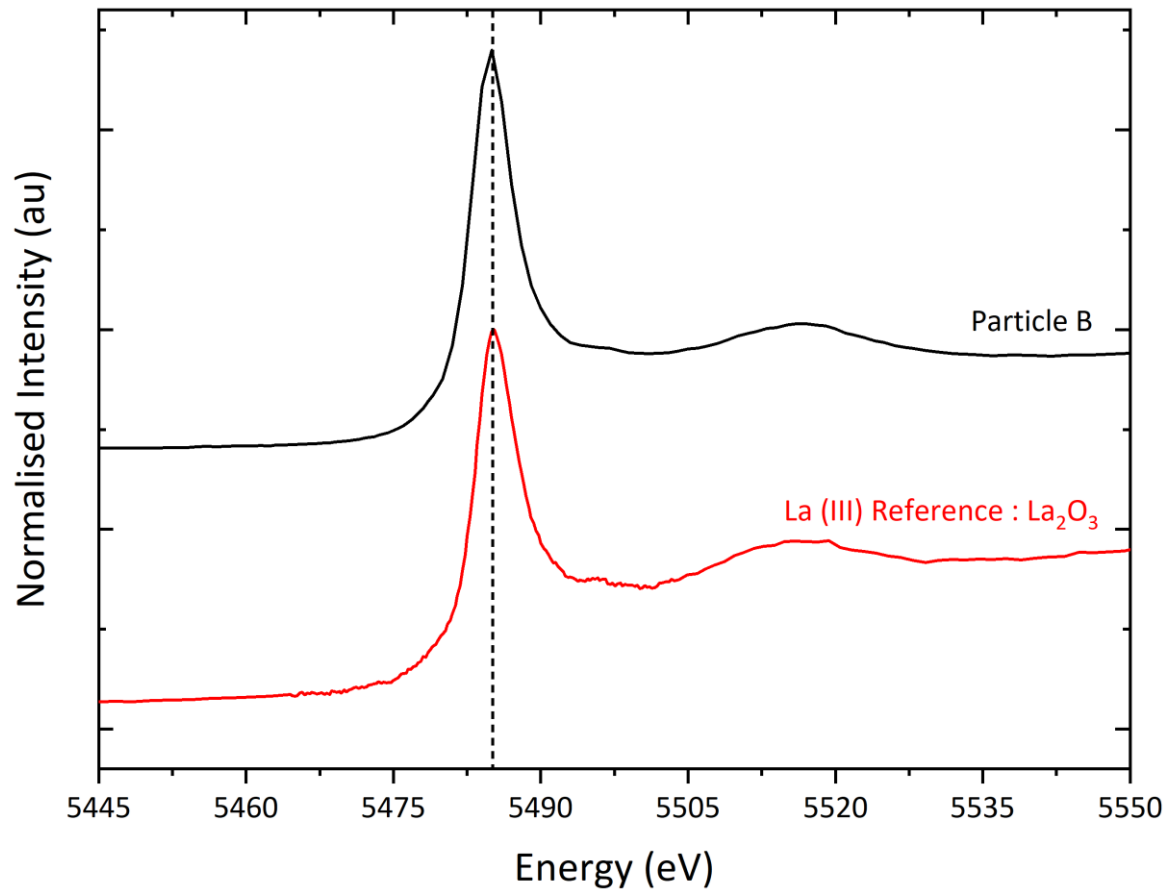


Fig. 8a: XANES spectrum of Ce in monazite particle **A** alongside its references [56]. Point P represents Ce (III) peak, and points Q and R represents Ce (IV) peaks.

Table 2: LCF results of Ce μ -XANES detailing the weight of Ce oxidation states.

	Component	Component weight (in % \pm uncertainty)	R-factor ^a
Particle A	CeTiO ₃ (Ce III)	80.2 \pm 0.044	0.038
	CeO ₂ (Ce IV)	19.8 \pm 0.062	
	Sum:	100	

^a R-factor defines the goodness of a fit, given as $\frac{\sum [(data-fit)^2]}{\sum (data^2)}$. Smaller R- factor represents a better fit.



465

466

Fig. 8b: XANES spectrum of La in monazite particle **A** alongside its reference [56].

1
2
3
4
5
6
7
8
9
10
11
12
13
14
15
16
17
18
19
20
21
22
23
24
25
26
27
28
29
30
31
32
33
34
35
36
37
38
39
40
41
42
43
44
45
46
47
48
49
50
51
52
53
54
55
56
57
58
59
60
61
62
63
64
65

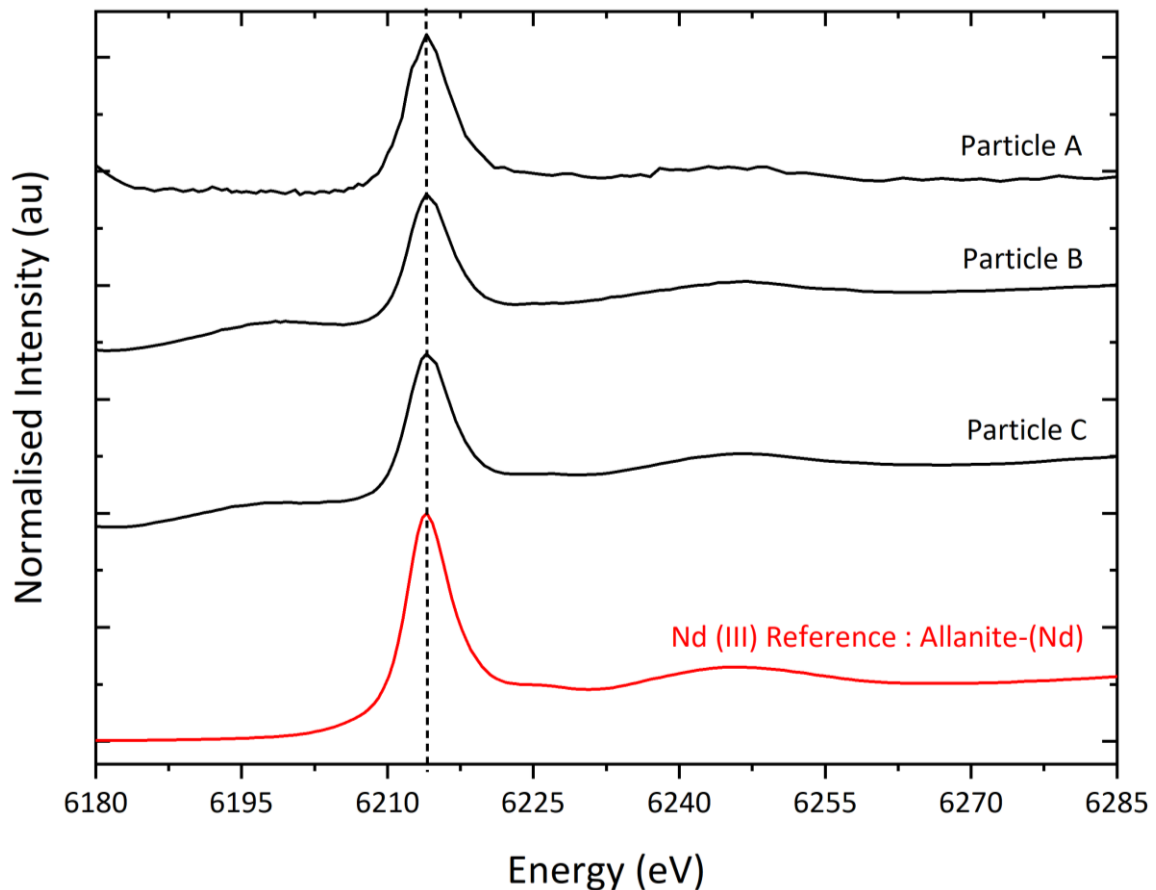


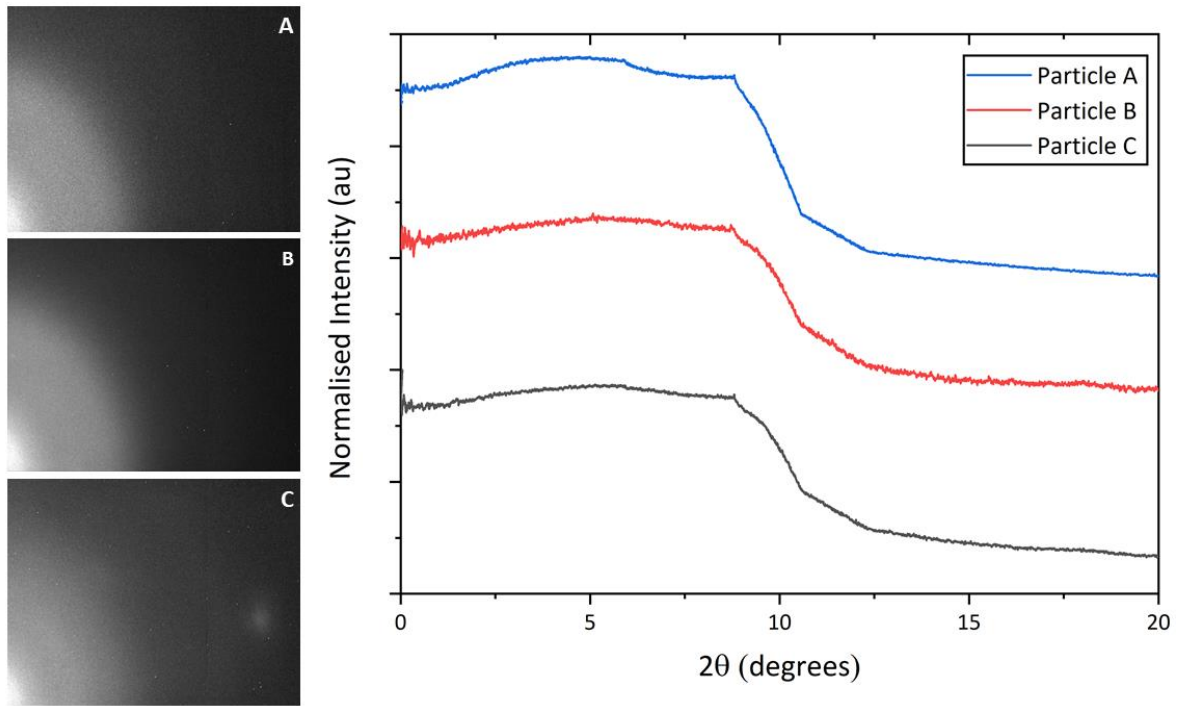
Fig. 8c: XANES spectrum of Nd in monazite particle **A**, **B** and **C** alongside its reference [56].

3.7 μ -XRD

The 2D and 1D μ -XRD patterns of particles **A**, **B** and **C** (Fig. 9) showed poorly formed diffuse diffraction rings, broad halo and lacking well-defined diffraction peaks, characteristic of amorphous materials. This implies partial or total amorphization/metamictization of the (naturally crystalline) monazite particle due to combined effects of alpha irradiation by uranium and thorium of the particles, combined with the high temperature ashing/combustion process. This radiation and/or high temperature induced structural transformation post combustion is vital in understanding the chemical reactivity, solubility and extractability of the REE from fly ash. Amorphization lowers the hardness of monazite thereby making it more susceptible to chemical attack with increased solubility. Monazite leaching can be done using a less aggressive dilute mineral acid at a lower temperature and in less time, which is more economical and with a higher REE extraction efficiency, than the conventional processes.

481

1
2
3
4
5
6
7
8
9
10
11
12
13
14
15
16
17
18
19
20
21
22
23
24
25
26
27
28
29
30
31
32
33
34
35
36
37
38
39
40
41
42
43
44
45
46
47
48
49
50
51
52
53
54
55
56
57
58
59
60
61
62
63
64
65



482

483 **Fig. 9:** 2D and 1D μ-XRD patterns of monazite particles **A, B** and **C**.

484 **4. Summary**

485 This work has determined the REE abundance and distribution in Nigerian fly ash. This knowledge is
486 essential to optimise the future REE recovery methods while simultaneously safeguarding the
487 environment from potential rare earth and heavy metal contamination, if released. Furthermore, this
488 study has also demonstrated a new method whereby individual monazite particles are removed from
489 bulk samples using an SEM-mounted micromanipulator (prior to synchrotron radiation analysis),
490 which has been demonstrated as being able to significantly enhance the resolution and quality of the
491 results obtained when compared to conventional ‘bulk’ characterisation methods.

492 The average total REE (plus Y and Sc) mass fractions in OMA, OKA and ODA fly ash samples were 623
493 mgkg⁻¹, 442 mgkg⁻¹ and 441 mgkg⁻¹, respectively. Additionally, analysis determined the existence of
494 dispersed (discrete) rare earth minerals (of detrital origin) with sizes between 10 μm and 70 μm in the
495 fly ash samples, with light REE in the monazite particles strongly colocalised and surface bound –
496 enveloping the actinides in a core-shell pattern. Ce was found to exist in mixed oxidation states (but

1 497 predominantly in the (III) oxidation state), with Nd and La being very stable in state III and unaffected
2 498 by the high temperature combustion process. Both U and Th were observed to be strongly colocalised,
3
4 499 were observed to be concentrated in the particle's interior and depleted around the circumference.
5
6
7 500 The monazite particles were metamict/amorphous which is attributed to irradiation and the high coal
8
9 501 combustion temperature. To the authors knowledge, such identification of elemental zonation within
10
11 502 isolated monazite particles derived from fly ash material represents the first complementary
12
13 503 synchrotron radiation μ -XRF and μ -XRF tomography study on coal fly ash. And while based only on an
14
15 504 indicative sample set, these initial results are very significant for the optimization and development of
16
17 505 rare earth extraction methods and represent a potentially highly valuable source for prized REE from
18
19 506 an otherwise pure waste product.
20
21
22
23

24 507 **Acknowledgements**

25
26
27
28 508 The authors wish to thank Diamond Light Source for rapid access to beamline I18 (SP22876) that
29
30 509 contributed to the results presented here. We also wish to thank the Commonwealth Scholarship
31
32 510 Commission for funding the PhD studentship.
33
34
35

36 511 **Appendix A. Supplementary data**

37
38
39 512 Supplementary data to this article can be found online at doi: ...
40
41

42 513 **Funding**

43
44
45 514 The SEM used in this work to conduct imaging and EDS analysis was purchased following funding by
46
47 515 the Engineering and Physical Sciences Research Council (EPSRC), (Reference: EP/K040340/1).
48
49
50

51 516 **Declarations of interest:** none.
52
53

54 517

55 518
56
57
58
59
60
61
62
63
64
65

519 **References**

- 1
2
3 520 [1] Xiaoyue Du and Graedel T. E. Global In-Use Stocks of the Rare Earth Elements: A First Estimate.
4
5 521 Environ. Sci. Technol., 45 (2011), pp. 4096–4101. [dx.doi.org/10.1021/es102836s](https://doi.org/10.1021/es102836s)
6
7 522 [2] BBC. Are rare earth minerals China’s trump card in its trade war with the US?
8
9 523 <https://www.bbc.com/news/amp/world-asia-48366074>, 2019 (accessed 30 May 2019).
10
11 524 [3] British Geological Survey (BGS). Rare earth elements.
12
13
14 525 www.MineralsUK.com, 2011 (accessed 18 July 2019).
15
16 526 [4] Asian Metals. Rare earth minerals and classification.
17
18
19 527 <http://metalpedia.asianmetal.com>, 2019 (accessed 6 July 2019).
20
21 528 [5] Weng, Z. H., Jowitt, S. M., Mudd, G. M., Haque, N. Assessing rare earth element mineral
22
23 529 deposit types and links to environmental impacts. *Trans. Inst. Min. Metall., Sect. B.*, 122 (2013),
24
25 530 pp. 83–96. DOI 10.1179/1743275813Y.0000000036
26
27 531 [6] Jordens, A., Cheng, Y. P., Waters, K. E. A review of the beneficiation of rare earth element
28
29 532 bearing minerals. *Miner. Eng.*, 41 (2013), pp. 97–114.
30
31 533 <http://dx.doi.org/10.1016/j.mineng.2012.10.017>
32
33 534 [7] Wedepohl, K. H. The composition of the continental crust. *Geochim. Cosmochim. Acta*, 59
34
35 535 (1995), pp. 1217–1232. [https://doi.org/10.1016/0016-7037\(95\)00038-2](https://doi.org/10.1016/0016-7037(95)00038-2)
36
37 536 [8] Ross K. Taggart, James C. Hower, Gary S. Dwyer, and Heileen Hsu-Kim. Trends in the Rare Earth
38
39 537 Element Content of U.S.-Based Coal Combustion Fly Ashes. *Environ. Sci. Technol.*, 50 (2016),
40
41 538 pp. 5919–5926. DOI:10.1021/acs.est.6b00085.
42
43 539 [9] Kanazawa, Y.; Kamitani, M. Rare earth minerals and resources in the world. *J. Alloys Compd.*,
44
45 540 408–412 (2006), pp. 1339–1343. <http://dx.doi.org/10.1016/j.jallcom.2005.04.033>
46
47 541 [10] US senate committee on energy & natural resources. Manchin, Capito & Murkowski
48
49 542 Reintroduce Rare Earth Element Advanced Coal Technologies Act.
50
51
52 543 www.energy.senate.gov, 2019 (accessed 6 May 2019).
53
54 544 [11] Mardon, S. M.; Hower, J. C. Impact of coal properties on coal combustion by-product quality:
55
56 545 examples from a Kentucky power plant. *Int. J. Coal Geol.*, 59 (2004), pp. 153–169.
57
58 546 [http://dx.doi.org/10.1016/S0166-5162\(04\)00033-3](http://dx.doi.org/10.1016/S0166-5162(04)00033-3)
59
60
61
62
63
64
65

- 547 [12] Hower, J. C.; Ruppert, L. F.; Eble, C. F. Lanthanide, yttrium, and zirconium anomalies in the Fire
1 Clay coal bed, Eastern Kentucky. *Int. J. Coal Geol.*, 39 (1999), pp. 141–153.
2
3 549 [https://doi.org/10.1016/S0166-5162\(98\)00043-3](https://doi.org/10.1016/S0166-5162(98)00043-3)
4
5
6 550 [13] Seredin, V. V.; Dai, S. Coal deposits as potential alternative sources for lanthanides and yttrium.
7
8 551 *Int. J. Coal Geol.*, 94 (2012), pp. 67–93. DOI: 10.1016/j.coal.2011.11.001
9
10 552 [14] Seredin, V. V. Rare earth element-bearing coals from the Russian Far East deposits. *Int. J. Coal*
11
12 553 *Geol.*, 30 (1996), pp. 101–129. [https://doi.org/10.1016/0166-5162\(95\)00039-9](https://doi.org/10.1016/0166-5162(95)00039-9)
13
14 554 [15] National Energy Technology Laboratory, U.S. Department of Energy. Characterization of Rare
15
16 555 Earth Element Minerals in Coal Utilization By-products.
17
18
19 556 <https://edx.netl.doe.gov/dataset/characterization-of-rare-earth-element-minerals-in-coal->
20
21 557 [utilization-byproducts](https://edx.netl.doe.gov/dataset/characterization-of-rare-earth-element-minerals-in-coal-), 2017 (accessed 8 May 2019).
22
23 558 [16] National Energy Technology Laboratory, U.S. Department of Energy. Rare Earth Element, 2019
24
25 559 project portfolio.
26
27 560 <https://netl.doe.gov/sites/default/files/2019-04/2019-REE-Project-Portfolio.pdf>, 2019
28
29 561 (accessed 2 July 2019).
30
31 562 [17] Hood M.M., Targgart R.K., Smith R.C., Hsu-Kim H., Henke K.R., Graham U., Groppo J.G., Unrine
32
33 563 J.M., Hower J.C. Rare earth element distribution in fly ash derived from the Fire Clay coal,
34
35 564 Kentucky. *Coal Combust. Gasificat. Products*, 9 (2017), pp. 22-33. doi: 10.4177/CCGP-D-17-
36
37 565 00002.1
38
39 566 [18] Hower J.C., Eble C.F., Dai S., Belkin H.E. Distribution of rare earth elements in eastern Kentucky
40
41 567 coals: indicators of multiple modes of enrichment? *Int. J. Coal Geol.*, 160-161 (2016), pp. 73-
42
43 568 81. DOI: 10.1016/j.coal.2016.04.009
44
45 569 [19] Montross S., Circe A.V., Falcon A., Poston J., Mark M. Characterization of rare earth element
46
47 570 minerals in coal utilization by-products and associated clay deposits from Appalachian Basin
48
49 571 coal resources. 34th International Pittsburgh Coal Conference Pittsburgh, PA. (2017).
50
51 572 [20] Newville M. Fundamentals of XAFS. Consortium for Advanced Radiation Sources, University of
52
53 573 Chicago, Chicago, IL. (2004).
54
55 574 [21] Smith J.V., Rivers M.L., Potts P.J., Bowles J.F.W., Reed S.J.B., Cave M.R. Synchrotron X-ray
56
57 575 microanalysis, *Microprobe Techniques in the Earth Sciences*, Springer US, Boston, MA, (1995),
58
59 576 pp. 163-233
60
61
62
63
64
65

- 577 [22] Takahashi Y., Shimizu H., Usui A., Kagi H., Nomura M. Direct observation of tetravalent cerium
1 578 in ferromanganese nodules and crusts by X-ray-absorption near-edge structure (XANES).
2
3 579 Geochim. Cosmochim. Acta, 64 (2000), pp. 2929-2935
4
5
6 580 [23] Takahashi Y., Sakami H., Nomura M. Determination of the oxidation state of cerium in rocks
7
8 581 by Ce LIII-edge X-ray absorption near-edge structure spectroscopy. Anal. Chim. Acta, 468
9
10 582 (2002), pp. 345-354. [https://doi.org/10.1016/S0016-7037\(00\)00403-8](https://doi.org/10.1016/S0016-7037(00)00403-8)
11
12 583 [24] Mengling Y. Stuckman, Christina L. Lopano, Evan J. Granite. Distribution and speciation of rare
13
14 584 earth elements in coal combustion by-products via synchrotron microscopy and spectroscopy.
15
16 585 International Journal of Coal Geology, 195 (2018), pp. 125-138.
17
18 586 <https://doi.org/10.1016/j.coal.2018.06.001>
19
20 587 [25] Pan Liu, Rixiang Huang, Yaunzhi Tang. Comprehensive understandings of rare earth element
21
22 588 (REE) speciation in coal fly ashes and implication for REE extractability. Environmental science
23
24 589 and technology, 53 (2019), pp. 5369-5377. DOI: 10.1021/acs.est.9b00005
25
26 590 [26] Thibault Cheisson and Eric J. Schelter. Rare earth elements: Mendeleev's bane, modern
27
28 591 marvels. Science 363 (2019), pp. 489–493. DOI: 10.1126/science.aau7628
29
30 592 [27] Ilemona C. Okeme, Thomas B. Scott, Peter G. Martin, Yukihiko Satou, Theophilus I. Ojonimi,
31
32 593 Moromoke O. Olaluwoye. Assessment of the mode of occurrence and radiological impact of
33
34 594 radionuclides in Nigerian coal and resultant post-combustion coal ash using scanning electron
35
36 595 microscopy and gamma-ray spectroscopy. Minerals, 10 (2020),
37
38 596 <https://doi.org/10.3390/min10030241>.
39
40 597 [28] Onoduku, Usman Shehu. Geochemical Evaluation of Okaba (Odagbo) Coal Deposit, Anambra
41
42 598 Basin, Nigeria. RJSITM, 03 (2014), ISSN: 2251-1563
43
44 599 [29] Ministry of Solid Minerals Development, Federal Republic of Nigeria. Feasibility Study:
45
46 600 Nigerian Coal Resource Development. <https://electricityinnigeria.com/>, 2006 (accessed 18
47
48 601 March 2019).
49
50 602 [30] Afu D.J., Ifeola E.O. and Adesida P.A. Omelewu coal characterisation for powering power plant
51
52 603 at Dangote cement factory, Obajana, Kogi state, Nigeria. American journal of engineering
53
54 604 research, 7 (2018), pp. 143-152. e-ISSN: 2320-0847.
55
56 605 [31] Mohammed U. Garba, Umaru Musa, Priscilla E. Azare, Kariim Ishaq, Usman S. Onoduku,
57
58 606 Yahaya S. Mohammad. Characterisation and ash chemistry of selected Nigerian coals for solid
59
60 607 fuel combustion. Petroleum and coal, 58 (2016), pp. 646-654. ISSN: 1337-7027.
61
62
63
64
65

- 608 [32] Chukwu M., Folayan C.O., Pam G.Y., Obada D.O. Characterisation of some Nigerian coals for
1 power generation. *Journal of combustion*, 2016.
2
3
4 610 <http://dx.doi.org/10.1155/2016/9728278>.
5
6
7 611 [33] energy mix report. ETA-ZUMA launches coal briquette production plant-Kogi state.
8
9 612 www.energymixreport.com/eta-zuma-launches-coal-briquette-production-plant-kogi/, 2018
10 (accessed 7 June 2018).
11 613
12
13 614 [34] Franklin Alli. Cement Manufacturers Cut Power Cost with Investments in Coal.
14
15 615 www.vanguardngr.com/2017/11/cement-manufacturers-cut-power-cost-coal-investments/,
16 2017 (accessed 8 June 2018).
17 616
18
19 617 [35] The Presidency, Federal Republic of Nigeria. National energy policy.
20
21
22 618 www.energy.gov.ng/, 2003 (accessed 12 July 2019).
23
24 619 [36] Pulverised coal combustion (PCC). [https://www.iea-coal.org/pulverised-coal-combustion-](https://www.iea-coal.org/pulverised-coal-combustion-pcc/)
25 [pcc/](https://www.iea-coal.org/pulverised-coal-combustion-pcc/). (Accessed 4 January 2018).
26 620
27
28 621 [37] Carl-Dieter Garbe-Schönberg. Simultaneous determination of thirty-seven trace elements in
29
30 622 twenty-eight international standards by ICP-MS. *Geostandards newsletter*, 17 (1993) pp. 81-
31 97.
32 623
33
34 624 [38] Kleindiek Nanotechnik GmbH, 'MM3A-EM Micromanipulator product brochure', tech.rep.,
35 Reutlingen, Germany.
36 625
37
38 626 [39] Martin P.G., Griffiths I., Jones C.P., Stitt C.A., Davies-Milner M., Mosselmans J.F.W., Yamashiki
39 Y., Richards D.A., Scott T.B. In-situ removal and characterisation of uranium-containing
40 627 particles from sediments surrounding the Fukushima Daiichi Nuclear Power Plant.
41 *Spectrochimica Acta Part B: Atomic Spectroscopy*, 117 (2016), pp. 1-7.
42 628
43 <https://doi.org/10.1016/j.sab.2015.12.010>.
44 629
45
46 630
47
48 631 [40] Kleindiek Nanotechnik GmbH, 'SEM Glu product brochure'.
49
50
51 632 [41] Mosselmans J.F.W., Quinn P.D., Dent A.J. Cavill S.A., Moreno S.D., Peach A., Leicester P.J.,
52 Keylock S.J., Atkinson K.D., Rosell J.R., Gregory S.R. I18-The microfocus spectroscopy beamline
53 633 at the Diamond Light Source. *J. Synchrotron Radiat.*, 16 (2009), pp. 818-824,
54 10.1107/S0909049509032282.
55 634
56 635
57
58 636 [42] Basham, M., Filik, J., Wharmby, M.T., Chang, P.C.Y., El Kassaby, B., Gerring, M., Aishima, J.,
59
60
61
62
63
64
65

- 637 Levik, K., Pulford, B.C.A., Sikharulidze, I. et al. Data Analysis WorkbenCh (DAWN).
1
2
3 638 J. Synchrotron Rad. 22 (2015), pp. 853-858. doi:10.1107/S1600577515002283
4
5 639 [43] Thermo Fisher Scientific. Amira-Avizo Software: 3D visualization and analysis software. (2019).
6
7 640 [44] Ravel B. and Newville M. ATHENA, ARTEMIS, HEPHAESTUS: data analysis for X-ray absorption
8
9 641 spectroscopy using IFEFFIT. J. of synch. Rad., 12 (2005), pp. 537-541.
10
11 642 10.1107/S0909049505012719
12
13 643 [45] ASTM C618-19: Standard specification for coal fly ash and raw or calcined natural pozzolan for
14
15 644 use in concrete. <https://compass.astm.org/>. (Accessed 7 March 2018).
16
17 645 [46] Ross K. Taggart, James C. Hower, Gary S. Dwyer, Heileen Hsu-Kim. Trends in the rare earth
18
19 646 element content of U.S.-based coal combustion fly ashes. Environ. Sci. Technol., 50 (2016), pp.
20
21 647 5919-26. Doi: 10.1021/acs.est.6b00085
22
23 648 [47] Zhen Wang, Shifeng Dai, Jianhua Zou, David French, Ian T. Graham. Rare earth elements and yttrium
24
25 649 in coal ash from the Luzhou power plant in Sichuan, Southwest China: concentration,
26
27 650 characterisation and optimised extraction, 203 (2019), pp. 1-14
28
29
30 651 <https://doi.org/10.1016/j.coal.2019.01.001>.
31
32 652 [48] S.F. Dai, L. Zhao, J.C. Hower, M.N. Johnston, W.J. Song, P.P. Wang, S.F. Zhang. Petrology,
33
34 653 mineralogy, and chemistry of size-fractioned fly ash from the Jungar power plant, Inner
35
36 654 Mongolia, China, with emphasis on the distribution of rare earth elements. Energy
37
38 655 Fuel, 28 (2014), pp. 1502-1514. <https://doi.org/10.1021/ef402184t>
39
40 656 [49] Modal S., Ghar A., Satpati A.K., Sinharoy P., Singh D.K., Sharma J.N., Sreenivas T., Kain V.
41
42 657 Recovery of rare earth elements from coal fly ash using TEHDGA impregnated resin.
43
44 658 Hydrometallurgy, 185 (2019), pp. 93-101. <https://doi.org/10.1016/j.hydromet.2019.02.005>
45
46 659 [50] Mardon, S. M.; Hower, J. C. Impact of coal properties on coal combustion by-product quality:
47
48 660 examples from a Kentucky power plant Int. J. Coal Geol., 59 (2004), pp. 153–169.
49
50 661 DOI:10.1016/j.coal.2004.01.004
51
52 662 [51] J.C. Hower, J.G. Groppo, P. Joshi, S. Dai, D.P. Moecher, M. Johnston. Location of cerium in
53
54 663 coal combustion fly ashes: implications for recovery of lanthanides Coal Combust. Gasificat.
55
56 664 Prod. (2013b), pp. 73-78
57
58 665
59 666 [52] R.K. Taggart, J.C. Hower, G.S. Dwyer, H. Hsu-Kim Trends in the rare earth element content of
60
61 667 U.S.-based coal combustion fly ashes. Environ. Sci. Technol., 50 (2016), pp. 5919-5926.
62
63 668 <https://doi.org/10.1021/acs.est.6b00085>
64
65 669 [53] Pingitore Nicholas, Clague Juan, Gorski Daniel. Round top mountain rhyolite (Texas, usa), a
66
67 670 massive, unique Y-bearing-fluorite-hosted heavy rare earth element deposit. Journal of rare
68
69 671 earths, 32 (2014), [https://doi.org/10.1016/S1002-0721\(14\)60037-5](https://doi.org/10.1016/S1002-0721(14)60037-5).
70
71 672

1
2
3
4
5
6
7
8
9
10
11
12
13
14
15
16
17
18
19
20
21
22
23
24
25
26
27
28
29
30
31
32
33
34
35
36
37
38
39
40
41
42
43
44
45
46
47
48
49
50
51
52
53
54
55
56
57
58
59
60
61
62
63
64
65

673 [54] Cotton S. Lanthanide and actinide chemistry. Chichester, England: John Wiley and Sons; 2006.

674 [55] Elizabeth J. Catlos. Generalisations about monazite: implications for geochronologic studies.
675 American mineralogist, 98 (2013), pp. 819-832

676 [56] International X-ray Absorption Society, 'XAFS Materials Database'.
677 http://ixs.iit.edu/database/data/Farrel_Lytle_data/RAW/index.html. (Accessed 6 March
678 2019).

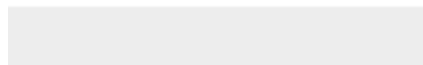


Click here to access/download
RDM Data Profile XML
renamed_23c6e.nxs



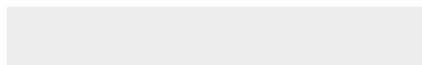


Click here to access/download
RDM Data Profile XML
renamed_c456d.nxs





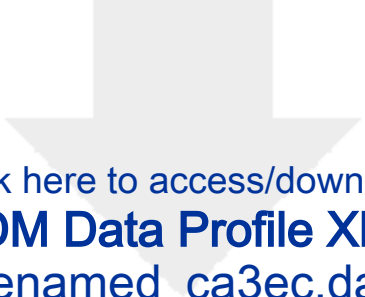
Click here to access/download
RDM Data Profile XML
renamed_05d36.nxs



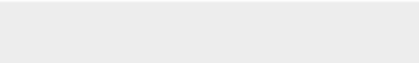



Click here to access/download
RDM Data Profile XML
renamed_07798.dat





Click here to access/download
RDM Data Profile XML
renamed_ca3ec.dat





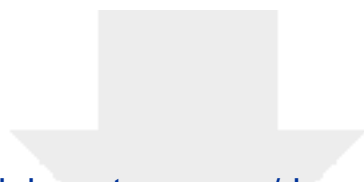
Click here to access/download
RDM Data Profile XML
renamed_43985.dat



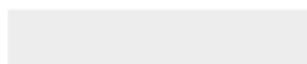


Click here to access/download
RDM Data Profile XML
renamed_538cb.dat





Click here to access/download
RDM Data Profile XML
renamed_4419d.dat





Click here to access/download
RDM Data Profile XML
renamed_f678e.nxs





Click here to access/download
RDM Data Profile XML
renamed_f8380.nxs



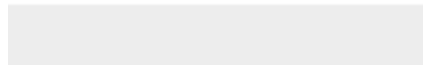


Click here to access/download
RDM Data Profile XML
renamed_82f7a.nxs



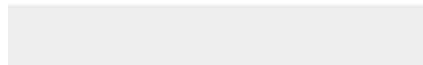


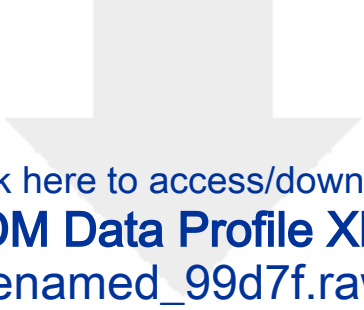
Click here to access/download
RDM Data Profile XML
renamed_092e4.raw






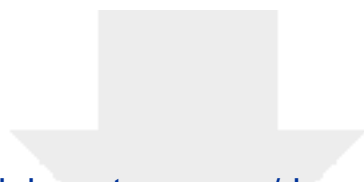
Click here to access/download
RDM Data Profile XML
renamed_e7784.raw



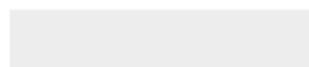


Click here to access/download
RDM Data Profile XML
renamed_99d7f.raw



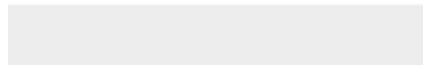


Click here to access/download
RDM Data Profile XML
renamed_37d8e.raw





Click here to access/download
RDM Data Profile XML
renamed_2511d.raw



Declaration of interests

The authors declare that they have no known competing financial interests or personal relationships that could have appeared to influence the work reported in this paper.

The authors declare the following financial interests/personal relationships which may be considered as potential competing interests:

Ilemona Okeme and **Thomas Scott**: Conceptualization, Methodology. **Ilemona Okeme**, **Peter Martin**, **Konstantin Ignatyev**, **Christopher Jones** and **Richard Crane**: Software, validation, Data curation, Investigation, Formal analysis, Visualisation, Writing- Original draft preparation. **Ilemona Okeme** and **Theophilus Ojonimi**: Resources. **Ilemona Okeme** and **Peter Martin**: Writing- Reviewing and Editing.



[Click here to access/download](#)

Supplementary Material

[Supplementary Figures and tables_SAP.docx](#)

